Global and Planetary Change 233 (2024) 104361

Contents lists available at ScienceDirect

Global and Planetary Change

journal homepage: www.elsevier.com/locate/gloplacha

Integrated cyclostratigraphy of the Cau core (SE Spain) - A timescale for climate change during the early Aptian Anoxic Event (OAE 1a) and the late Aptian

Rafael Martínez-Rodríguez [a,b,*], Sietske J. Batenburg [c], José M. Castro [a], Ginés A. de Gea [a], Luis M. Nieto [a], Pedro A. Ruiz-Ortiz [a], Stuart Robinson [d]

[a] CEACTEMA and Geology Department, University of Jaén, Campus Universitario, 23071 Jaén, Spain
[b] GEODESPAL Department (Geodynamics, Stratigraphy and Paleontology), Faculty of Geological Sciences, Complutense University, Madrid, C/ José Antonio Novais, 12, 28040 Madrid, Spain
[c] Facultat de Ciències de la Terra, Universitat de Barcelona, Martí i Franqués, 08028 Barcelona, Spain
[d] Department of Earth Sciences, University of Oxford, South Parks Road, Oxford OX1 3AN, UK

ARTICLE INFO

Editor: Dr. Alan Haywood

Keywords:
Cyclostratigraphy & astrochronology
Aptian
OAE 1a
Time-series analysis
Paleoclimatology

ABSTRACT

We report a cyclostratigraphic study performed on the Cau core (Spain), which is considered an Aptian stratigraphic reference for global correlation and paleoenvironmental reconstruction. This investigation presents an astronomical timescale for the Aptian from the Ap2a to Ap14 carbon-isotope stages. Based on the evaluation of a multiproxy dataset from the Cau core, we recalibrate the age and duration of different biozones, bioevents, chemostratigraphic substages and horizons from the early and late Aptian, with special focus on the Selli Event, providing a new astronomical framework for Aptian climate. From the recognition of 14 long-eccentricity cycles, we propose a time span of 5.67 Ma from C-isotope segments Ap2a to the top of Ap14, and ages of 120.82 Ma for the onset of the nannoconid crisis, and 120.20 Ma for the onset of oceanic anoxic event (OAE) 1a. Calculations yield a duration of 1.47 Ma for OAE 1a. We estimate the age for the onset of the main non-radiogenic phase of the Os isotopes at 120.08 Ma, 120 ka after the onset of OAE 1a. The high-resolution data from the Cau core provide further insights in the temporal constraints of the OAE 1a and other Aptian paleoclimatic events. The onset of the main non-radiogenic excursion in Os isotopes occurring 120 ka after the onset of OAE 1a reinforces the theory of rapid destabilization of methane hydrates as the trigger of the anoxic event, that preceded the onset of large-scale volcanism.

1. Introduction

The Aptian-Turonian interval was characterized by intermittent super-greenhouse conditions and a warm climate, with an absence of ice sheets and weak latitudinal temperature gradients (Bodin et al., 2015; Föllmi, 2012; Friedrich et al., 2012; O'Brien et al., 2017). During the Aptian (121.4 to 113.2 Ma; Gradstein et al., 2020), temperatures and sea-levels oscillated, with a major rise in both during the early Aptian. Recurrent anoxic conditions in the Tethys Ocean and worldwide led to the deposition of several organic-rich beds, including the Selli, Noir, Fallot, and Jacob levels (e.g., Ando et al., 2017; Bréhéret, 1994, 1995; Caillaud et al., 2020, 2022; Ferry, 2017; Friedrich et al., 2003; Friès and Parize, 2003; Heimhofer et al., 2004, 2006; Herrle et al., 2003, 2004, 2010; Rubino, 1989; Stein et al., 2011; Tribovillard, 1989; Tribovillard and Gorin, 1991; Westermann et al., 2013). One of the intensely studied Oceanic Anoxic Events (OAEs) is the early Aptian OAE (OAE 1a) (see Arthur et al., 1990; Erba et al., 1999, 2015; Méhay et al., 2009; Stein et al., 2011). The most distinct feature of this event is a negative excursion in carbon isotope values, followed by a pronounced positive excursion. The positive and negative shifts in $\delta^{13}C$ have been observed worldwide and both in terrestrial and marine records (e.g., Ando et al., 2008; Bralower et al., 1999; Castro et al., 2021; De Gea et al., 2003; Elkhazri et al., 2013; Gröcke et al., 1999; Heldt et al., 2008; Hu et al., 2012; Kuhnt et al., 2011). Although OAE 1a has been extensively studied with many studies focused on environmental changes, the pacing of the event itself is poorly constrained, leading to uncertainty regarding the

* Corresponding author at: CEACTEMA and Geology Department, University of Jaén, Campus Universitario, 23071 Jaén, Spain.
E-mail addresses: rodrigue@ujaen.es, rafaelma@ucm.es (R. Martínez-Rodríguez).

https://doi.org/10.1016/j.gloplacha.2024.104361
Received 5 August 2022; Received in revised form 18 December 2023; Accepted 12 January 2024
Available online 16 January 2024

causal mechanisms (Adloff et al., 2020). Although it is considered that OAE 1a was characterized by a major warming, there is some evidence that cooler intervals or "cold snaps" occurred during the event (e.g., Jenkyns, 2018). Three possibly global cooling episodes have been documented within OAE 1a through high-resolution studies. Cooling has been tentatively related to reduced atmospheric CO_2 levels (Jenkyns, 2018) possibly resulting from lessened volcanic activity in combination with an increase in global burial of organic matter (Gröcke et al., 1999; Skelton and Gili, 2012) and accelerated silicate weathering on the continents (Archer, 2011; Berner, 2004).

Despite its rich sedimentary record of environmental change, a complete picture of climatic evolution during the Aptian is not available, because most successions cover only limited portions of the Aptian stage (Li et al., 2008; Lorenzen et al., 2013; Malinverno et al., 2010). In particular, the middle and late Aptian lack a sufficiently constrained chronology, limiting paleoclimatic studies.

Unravelling the sequence of events leading to episodes of oceanic anoxia requires constraints on the tempo and mode of climate change by studies of well-dated sedimentary successions. The newly drilled Cau core in south-eastern Spain presents an exceptional archive of past environmental change during the early and late Aptian. The Cau Core is particularly suitable for the study of OAE 1a as it provides an expanded succession from a relatively shallow marine environment, in comparison to other deeper and/or condensed sections from the Tethyan domain. The objective of this work is to analyse and study the cyclostratigraphic data from the Cau core to establish a floating timescale for the Aptian stage, with particular interest in OAE 1a.

1.1. Aptian timescale

The Aptian is the third-longest stage in the Cretaceous, and the durations and timings of its main events are still under debate (Erba et al., 2015). A duration for the Aptian stage of 13.4 Ma was suggested by an astrochronology from the Piobbico core which recovered 33.7 m of the Fucoid marls near Piobbico, central Italy (Huang et al., 2010). Scott (2014) sets a duration of the Aptian of about 12 Ma, while the duration estimates in the International Chronostratigraphic Chart (ICC - Cohen et al., 2013; v2023/04) and the GTS2020 (Gradstein et al., 2020) for the Aptian stage are 8.4 and 8.2 Ma, respectively. A study from the Umbria-Marche Basin (Italy) has proposed a shorter timespan for the Aptian of ~7.2 Ma (Leandro et al., 2022), whereas other study from the Vocontian Basin (SE France) proposes a timespan of ~9.4 Ma (Charbonnier et al., 2023). The former studies show the high variability in estimations of the duration of the Aptian stage.

Concerning the Aptian boundaries and events, a proposal is underway to define the base of the Aptian with a Global Boundary Stratotype Section and Point (GSSP) at the base of the Ap3/C3 carbon isotope segment, with the Cau section amongst the candidate localities (Castro, pers. comm.). Meanwhile, different definitions of the stage boundaries and differences in dating efforts result in a range of ages and durations suggested for the Aptian and OAE 1a. The base of the Aptian is set at ~121.4 Ma in the ICC (Cohen et al., 2013; v2023/04)), and the GTS2020 (Gradstein et al., 2020) provides an age of 121.4 ± 0.6 Ma for the Barremian/Aptian boundary (Zhang et al., 2021). This age is in close agreement with a published cyclostratigraphic calibration of the Barremian (Martinez et al., 2020), suggesting an age for the Barremian/Aptian boundary of 121.40 ± 0.34 Ma, updated to 121.15 ± 0.31 Ma (Martinez et al., 2023). Charbonnier et al. (2023) proposed a duration of the Aptian Stage of 9.4 Ma and an age of 122.6 ± 0.3 Ma for the base of the Aptian. The top of the Aptian is set at ~113.0 Ma in the ICC (Cohen et al., 2013; v2023/04) and at 113.2 ± 0.3 Ma in the GTS2020 (Gradstein et al., 2020), based on a U–Pb date of a basal Albian volcanic ash layer in north-west Germany (Selby et al., 2009). Several studies have focused on estimating the duration of OAE 1a in the early Aptian, including Li et al. (2008), Huang et al. (2010), Malinverno et al. (2010), Ogg and Huang, 2012 Scott (2014), Moullade et al. (2015), Scott (2016), Leandro et al. (2022), and Charbonnier et al. (2023) resulting in estimated durations ranging from 0.56 to 1.5 Ma.

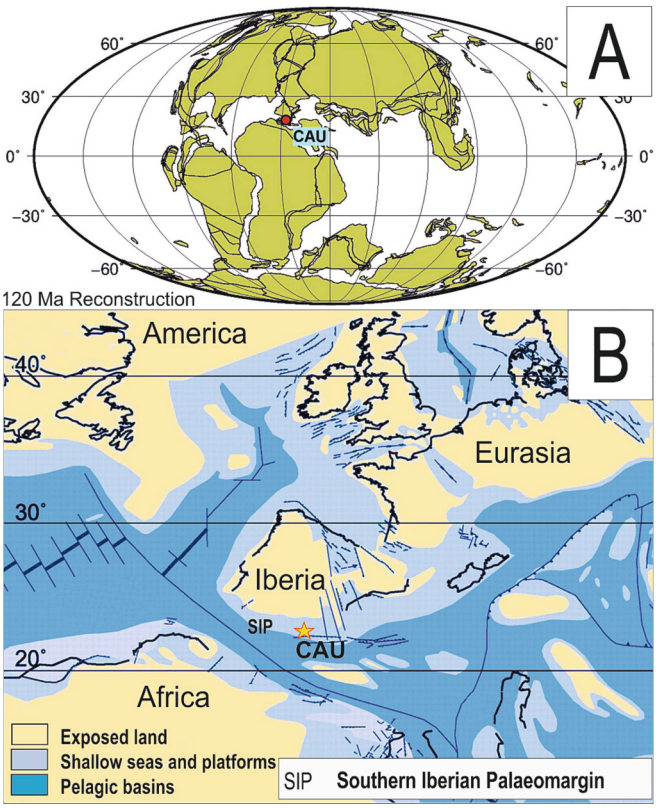

Fig. 1. A. Palaeogeographic reconstruction (based on www.osdn.de; Hay et al., 1999) for the Early Aptian (120 Ma) showing the location of the Cau section. B. Palaeogeography of the Iberian Plate during the Aptian (simplified from Masse et al., 1993).

2. Geological setting and earlier work

The Cau Core was drilled during 2015–2016 in the Cau section (Latitude: 38.70389°N - Longitude: 0.00472°W), located in the SE of Spain, in the province of Alicante. Four boreholes were drilled (Fig. 2) in the Cau hill to obtain an almost continuous record of the Almadich Formation (Fm) (Castro et al., 2019; Ruiz-Ortiz et al., 2016). The drilled materials of the core from the Cau hill have a mean dip angle of 20^0, but some sections display 10^0 of dip while others have 30^0, so a dip correction was applied over 5 m intervals. Hole D4 overlaps D3 by 15.4 m, D3 and D2 overlap by 6.4 m, there is no overlap between D1 and D2, and a gap of 1 m has been assigned. For a more detailed report on the extraction, logging, biostratigraphy, and lithology of the core see Ruiz-Ortiz et al., (2016) and Castro et al. (2021). At Cau (SE Spain), hemipelagic marls with varying amounts of organic carbon were deposited in a tropical climate at a palaeolatitude of about 22.5°N (Fig. 1A-B), on a margin that experienced extensional rifting as the Western Tethys was opening (Castro et al., 2019; De Gea et al., 2003; Naafs et al., 2016). Palaeographically, the area is in the Southern Iberian Palaeomargin (SIP) (Fig. 1B), which is currently positioned in the Prebetic (Betic External Zones) (Martín-Chivelet et al., 2019; Vera, 2001; Vera, 2004). The Aptian succession of the Almadich Fm at Cau is composed by marls, with intercalated beds of marly limestones less than one-meter thick (Fig. 3). Alternations between marls and limestones are more easily observed in the field than in the core. The materials represent the distal expression of a shallow carbonate ramp with hemipelagic sedimentation. During OAE 1a, laterally equivalent shallow carbonate platform materials from the eastern sector of the Aptian Prebetic platform were

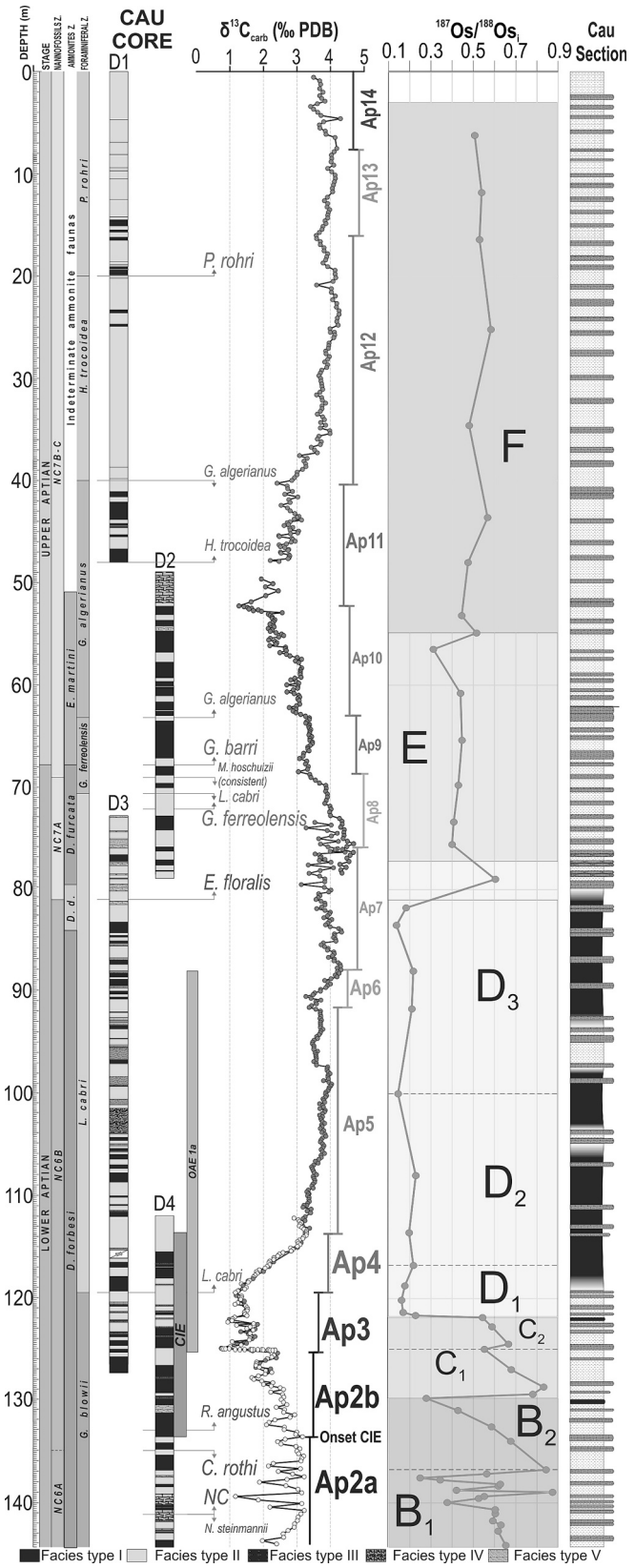

(caption on next column)

Fig. 2. Bulk-carbonate carbon and oxygen isotope data from Cau composite core against depth, and the Cau outcrop section (from Naafs et al., 2016). CIE-Carbon Isotope Excursion; OAE 1a-Oceanic Anoxic Event 1a. Segments of $\delta^{13}C$ chemostratigraphy (Ap2-Ap14) follow the nomenclature by Castro et al. (2021). Stratigraphic profile of Os isotope ratios from Martínez-Rodríguez et al., (2021). Facies description: (I) Dark grey massive facies, locally with faint lamination and scarce bioturbation. (II) Light grey bioturbated facies, the intensity of bioturbation is highly variable. (III) Dark grey undisturbed mudstones with planar lamination. (IV) Light to dark grey brecciated to nodular facies with chaotic organization and massive mudstone/wackestone texture irregularly interbedded with partially recrystallized limestone. (V) Grey to orange, weathered, recrystallized, or altered facies.

drowned under a transgressive regime (Castro et al., 2008; Martínez-Rodríguez et al., 2018; P. W. Skelton et al., 2019).

2.1. Biostratigraphy

The record of the Cau Core begins in nannofossil Subzone NC6A (Fig. 2), with the nannofossil markers *Hayesites irregularis, Nannoconus truittii and Conusphaera rothii* found at the base of the core. Also recorded in the lowermost part of the core is the highest occurrence (HO) of *Nannoconus steinmanii*, which represents the "nannoconid crisis" event (Fig. 2). The identification of the nannoconid crisis and the absence of *Leupoldina cabri* allows us to situate the base of the core within the planktonic foraminifera biozone of *Globigerinelloides blowi*. The Cau Core ranges through the Aptian until the *Paraticinella rohri* zone, in the uppermost part of the NC7 zone. The biostratigraphic information provides a framework for a first order estimate of sedimentation rate variability across the cored interval (Table 1).

Estimated sedimentation rates vary according to the ages applied by different authors, with the starkest difference for the planktic foraminifera (Fig. 4, Table 1). The main difference in the sedimentation rate tendency from the two provided planktonic foraminifer zone age sets is found in the *Hedbergella trocoidea* zone, with estimated sedimentation rates of 10.00 cm/ka (using ages from Gradstein et al., 2020) and 4.17 cm/ka (using ages from Malinverno et al., 2010) (Fig. 4, Table 1). This comes from differences in timespan for the *H. troicoidea* zone between the two chronologies, spanning 0.2 Ma in Gradstein et al., (2020) and 0.48 Ma in Malinverno et al., (2010). However, this biozone only spans 20.0 m of the 144.4 m long series. The Cau Core is biostratigraphically complete, yielding a weighted average sedimentation rate of 5.42 cm/ka (forams) and 2.45 cm/ka (ammonites) for the early Aptian, whereas for the late Aptian, the sedimentation rate is 0.98 cm/ka (forams) (Fig. 4). The sedimentation rate was generally higher in the early Aptian than in the late Aptian, due to a decrease in regional rifting activity (Castro et al., 2021).

2.2. Chemostratigraphy and correlation

Stable carbon-isotope ratios of bulk carbonates were analysed at a ~30 cm resolution throughout the four individual cores to generate a composite record (Castro et al., 2021). Fig. 2 shows 755 values along the 144.4 m composite of the Cau Core. To provide an Os-isotope record for the entire Cau section, 56 samples were collected, between the base and top of the Cau section (Fig. 2) (Martínez-Rodríguez et al., 2021). The composite record of the core has been constructed comparing the gamma ray signal between cores, correlating the $\delta^{13}C$ data and faunal data from biostratigraphy.

3. Materials and methods

3.1. Natural gamma ray logging and magnetic susceptibility

Gamma Ray levels were measured with a wireline QL40 sensor probe at a 3 cm spacing and reported as API (American Petroleum Institute)

Table 1
Identified biozones in the Cau Core, with base and top depths, corresponding estimated ages from Malinverno et al., (2012), Coccioni (2019), Gradstein et al. (2020), and resulting sedimentation rates.

Foraminifera zones	Depth (m)	Ages from Gradstein et al., 2020 (Ma)	Sed. rate (cm/kyr)	Ages from Malinverno et al., 2010 & Coccioni, 2019* (Ma)	Sed. Rate (cm/kyr)
G. blowii	Base: 144.4 Top: 119.5	Base: 120.7 Top: 120.6	24.9		
L. cabri	Base: 119.5 Top: 70.6	Base: 120.6 Top: 118.6	2.45	Base: 120.80* Top: 118.74	2.37
G. ferroelensis	Base: 70.6 Top: 63.2	Base: 118.6 Top: 118.2	0.53	Base: 118.74 Top: 117.64	0.67
G. algerianus	Base: 63.2 Top: 40.0	Base: 118.2 Top: 116.8	1.66	Base: 117.64 Top: 115.74	1.22
H. trocoidea	Base: 40.0 Top: 20.0	Base: 116.8 Top: 116.6	10.00	Base: 115.74 Top: 115.26	4.17
P. rohri	Base: 20.0 Top: 0.0	Base: 116.6 Top: 114.2	0.83		

Ammonites zone	Depth (m)	GTS2020 Age (Ma)	Sedimentation rate (cm/kyr)
D. forbesi	Base: 144.4 Top: 84.4	Base: 120.7 Top: 120.0	8.57
D. deshayesi	Base: 84.4 Top: 79.9	Base: 120.0 Top: 119.1	0.50
D. furcata	Base: 79.9 Top: 67.9	Base: 119.1 Top: 118.8	4.00
E. martini	Base: 67.9 Top: 50.9	Base: 118.8 Top: 117.5	1.31

radioactivity units (Fig. 3). Magnetic Susceptibility (MS) was measured on the cut core-surface using a cylindrical Bartington MS2E core logging sensor device, with the BartSoft program. Measurements were performed manually at a 5 cm spacing under atmospheric conditions at 25 °C temperature. Each point was measured three times and averaged to reduce errors, and reported in IU (instrumental units), although the lower part of the data from 144.4 to 110 m has been removed due to measurement errors.

3.2. Carbonate content

The Cau Core has been sampled with a standard spacing of 10 cm for powder samples, and 250 to 300 mg of each sample was reacted with 5.3 M hydro-chloric acid. Emitted carbon dioxide was measured with an automatic calcimeter (DREAM Électronique SAS, Pessac, France) to determine the carbonate content.

3.3. Sedimentary cyclicity

To test for a potential orbital imprint on sedimentation at Cau, the high-resolution physical property and carbonate data were subjected to time series analyses. The program Redfit, designed to work with unevenly spaced series (v3.8e; Schulz and Mudelsee, 2002), was used to generate power spectra from the original data. The spectrum of the detrended series was calculated using the multi-taper method (2π-MTM spectrum; Thomson, 1982; Thomson, 1990).

Continuous wavelets transform, evolutive harmonic analysis and the Average Spectral Misfit (ASM) method (Meyers, 2019; Meyers and Sageman, 2007) were conducted using the Astrochron software package (v1.1; Meyers, 2019) in R·Studio (R Core Team, 2013), to investigate periodicities in the records. Scripts used in R, are available in Appendix C. Correlation coefficient (COCO) and evolutionary Correlation Coefficient (eCOCO) analyses were performed in Acycle (v2.6; Li et al., 2019). The core logging data were also analysed visually, integrating the observations with the facies lithology of the core, the biostratigraphic data and the stable isotope profiles to complement the spectral calculations.

4. Results

4.1. Sedimentary response

The Cau Core presents an alternation of light and dark colored bands or levels, usually on a decimeter scale. Marl levels are darker in colour, in contrast to limestone levels that have lighter tones. The expression of rhythmic marls/limestones is the result of the multi-million-year record of hemipelagic deposition in the distal part of the Prebetic carbonate ramp. An image of a limestone-marl alternation is shown in Appendix B, which displays a portion of the core and a micro-X-ray fluorescence (μ-XRF) mapping image. The limestone is enriched in Ca, whereas the marly part is enriched in other elements such as Al, Si, Ti, S, K, Fe, Sr and Zr. The marls have higher gamma ray values, higher MS values and lower $CaCO_3$ contents than the limestones (Fig. 3) (see also Figs. 1 and 3 in Appendix B).

4.2. Cyclicity

Time series analyses performed with Redfit are presented against MTM spectra to compare the results (Fig. 5). The redfit analyses were conducted on the original raw data, without subtracting the mean and detrending, as a first test of the reliability of detected periodicities. For the MTM analyses, data were linearly interpolated, and trends in the signals were subtracted using the LOWESS smoothing method

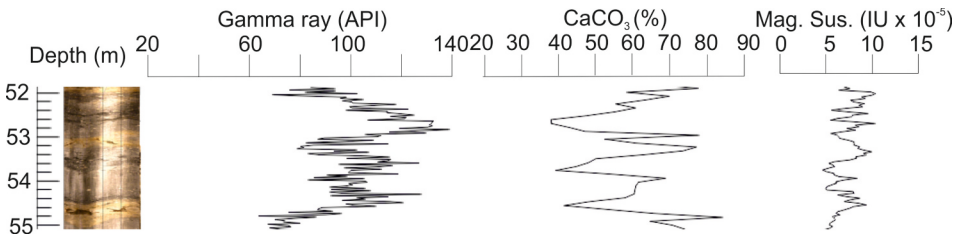

Fig. 3. 3-m interval of core lithology, gamma ray, $CaCO_3$ and MS. Three darker bands display higher values of gamma ray, MS, and lower values of calcium carbonate. Clear lithologic intervals show the opposite behaviour in the physical and chemical data, showing minima in gamma ray, MS, and maxima in $CaCO_3$. A complete image of proxies for the complete Cau Core can be found in Fig. 9 and in Appendix B (Fig. 1).

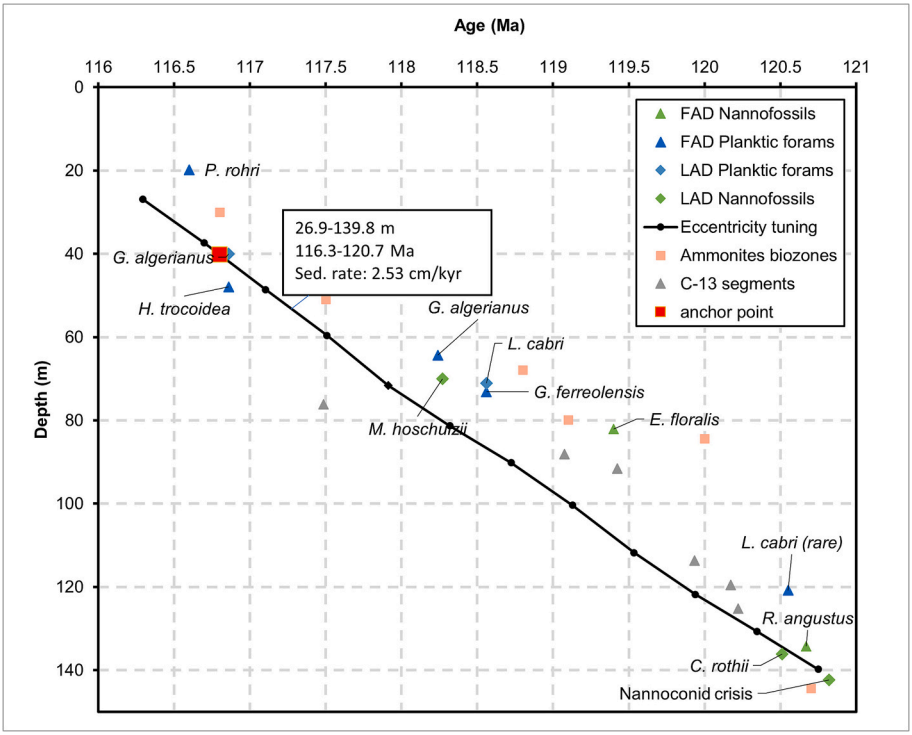

Fig. 4. Range of ages (Ma) for the different biozones from the Cau Core, listed in Table 1. FAD = first appearance datum; LAD = last appearance datum. Triangles with apex up represent FADs. Diamonds represent LADs. Planktic foraminifera from GTS2020 (Gradstein et al., 2020); ammonite zones from GTS2020; planktic foraminifera from Malinverno et al., 2010, and Coccioni et al., 2019; and $\delta^{13}C$ segments from Malinverno et al., 2010 are represented. In black dots, tie-points for the cyclostratigraphic model of this study.

(Cleveland, 1979). Then, the 20% LOWESS trends were calculated on the instantaneous amplitudes of the signals, using the Hilbert transform. The residual signals were divided by the long-term signal of the instantaneous amplitude, and then standardized, so that both the average and variance of the series are stationary. This detrend procedure allows the elimination of the lowest frequencies while not impacting higher frequencies or creating spurious frequencies in the lowest part of the spectrum (Ait-Itto et al., 2023). The red-noise modeling was calculated using the classic AR(1) method following Husson (2014).

The $CaCO_3$ content record reveals its main periodicities at 72, 10.28, and 0.35–0.37 m (above 99% confidence, Fig. 5A), in the redfit spectra. In the MTM spectra, 11.50, 0.80 and 0.36–0.37 m periodicities present a 99.9% level of confidence, and 0.88, 0.47, 0.43 and 0.40 m are above 99% (Fig. 5B). In the redfit spectra of the gamma-ray record, the main periodicities above 99% are at 35.93, 20.52, 13.1 and 5.76 m (Fig. 5C). In the MTM spectra, periodicities of 35.93 and 13.1 m are present a 99.9% confidence, and a 5.76 m periodicity is detected is above 99% confidence (Fig. 5D). In the redfit spectra of MS, the periodicities above 99% confidence are at 54.84 and 9.97 m (Fig. 5E). In the MTM spectra, the periodicities above 99.9% confidence are at 54.84 and 10.28 m, and a peak at 4.00–4.38 m reaches the 99% confidence level (Fig. 5F).

4.3. ASM, COCO and eCOCO

The ASM method is used to evaluate the main frequencies observed in the spectral analyses (>99% confidence) and to assess the data spectrum with an astronomical target spectrum for the Aptian (118 Ma), using the most stable components of eccentricity at 405-ka, 131-ka, 124-ka, 99-ka and 95-ka (see GTS2020 – chapter 4) and predicted orbital periods for obliquity (49.588-ka and 38.404-ka) and precession (22.156 and 18.392) from Berger et al. (1992). The optimal sedimentation rate obtained using a range from 0.5 to 24.9 cm/ka (Table 1) for the Cau core is 2.377 cm/ka (Fig. 6). COCO analysis for the gamma ray record, for a range of sedimentation rates from 1.00 to 20.00 cm/ka, exhibits two main maxima of stable sediment accumulation rate, at 3.33 cm/ka and 13.67 cm/ka (Fig. 6B), but the peak at 3.33 cm/ka exceeds the null hypothesis significance level (H_0, no orbital forcing) by one order of magnitude. COCO analysis for the MS record (from 110 m to top), for a range of sedimentation rates from 0.5 to 10 cm/ka, exhibits a main maximum at 2.36 cm/ka (Fig. 6C) surpassing the null hypothesis significance level (H_0, no orbital forcing). This MS result, although not for the complete record, are is in close agreement with the ASM result for the complete record (2.37 and 2.36 cm/ka respectively). The eCOCO results of the gamma ray record, tested for a range of 1.00 to 20.00 cm/ka with a window of 17.5 m (Appendix C). The evolutionary null hypothesis (H_0) significance level showed the lowest results by 1.5 to 3.0 cm/ka (Fig. 6D), lower than 0.02. COCO and eCOCO analyses of the $CaCO_3$ data resulted in similar outcomes (scripts in Appendix C) The COCO sedimentation rates are 3 and 11 cm/ka (Fig. 4 of Appendix B), but the eCOCO analysis indicates higher significance levels for lower sedimentation rates, roughly between 1 and 4 cm/ka (Fig. 5 of Appendix B). The target series used for both COCO and eCOCO is the La2004 astronomical solution (Laskar et al., 2004) at 118 Ma.

5. Discussion

The gamma ray and MS records mirror the $CaCO_3$ data (Fig. 3) (see also Fig. 2 from Appendix B), likely reflecting variations in the terrigenous input of clay leading to the deposition of marls, and in the supply of carbonate by marine productivity leading to the formation of limestones.

The marls contain higher concentrations of detrital elements Al, Si and Fe, while the limestones possess a higher Ca content (Appendix B – Fig. 3). The driver of the observed sedimentary cyclicity may be variations in the amount of run-off and weathering influencing the amount of clay input and carbonate productivity (Martinez et al., 2015; Moiroud et al., 2012). Climate variations forced by cyclic changes in the insolation pattern may have resulted in these alternations of limestones and

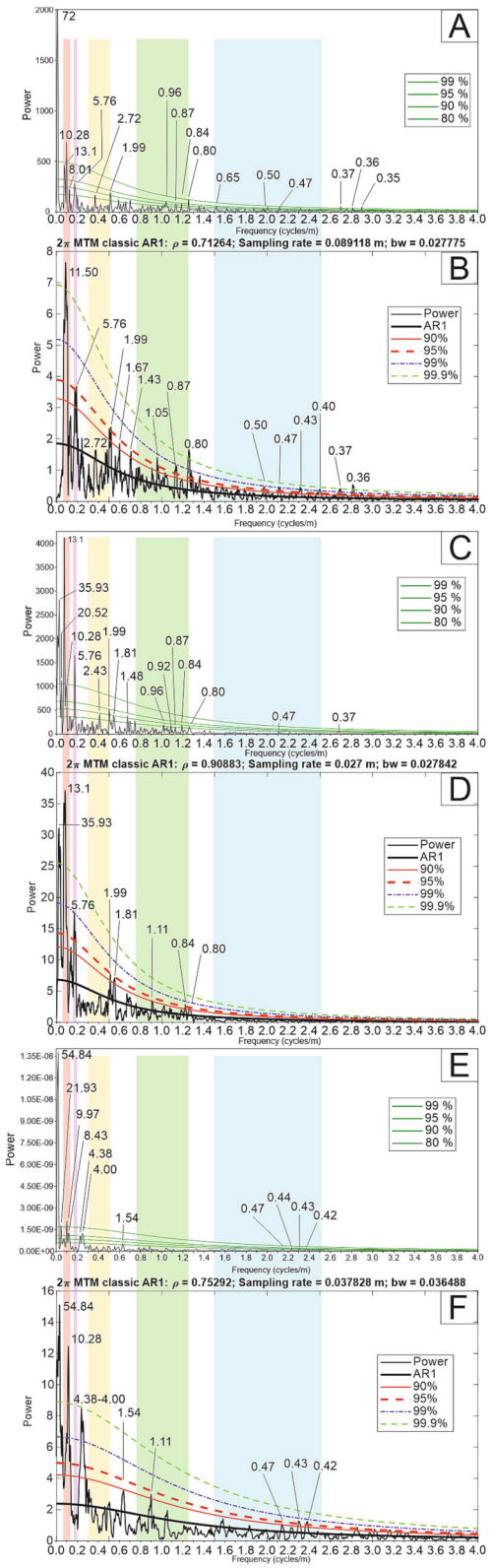

Fig. 5. Redfit power spectra (using a Welch window and a segment of 1) and three 2π prolate tapers (2π-MTM) of $CaCO_3$ (A-B), gamma ray (C–D) and magnetic susceptibility (E-F) for the whole interval. Periods are labelled in meters. Colour bands represent the ranges of astronomical parameters. The red band represents 405-ka eccentricity. Pink band: possible long obliquity modulation. Yellow band: 100-ka eccentricity. Green band: 40-ka obliquity. Blue band: 20-ka precession. (For interpretation of the references to colour in this figure legend, the reader is referred to the web version of this article.)

marls. This may be driven by changes in seasonality, with a high amplitude of precession causing increased seasonality and stronger monsoon-like precipitation and increased run-off and clay input (Batenburg et al., 2016). The higher sedimentation rate in the lower Aptian (~4 cm/ka) compared to the upper Aptian (~1 cm/ka) indicates more presence of siliciclastics in the lower Aptian, and more presence of carbonate in the upper Aptian.

According to independent biostratigraphic control and to spectral analyses, 405-ka periodicities may fall in the range of 8–13 m, with the Cau core encompassing 11 to 18 long eccentricity cycles. Periodicities above 99% confidence at 72, 54.84, 35.93, 21.93 and 20.52 m are too long to be evaluated in this study, and only the periodicity of 35.93 m found in the redfit and MTM spectra of gamma ray would represent the 1.2-Ma periodicity. Gamma ray, $CaCO_3$ and MS follow the lithological banding patterns, showing alternations on various spatial scales (Fig. 7). Collectively, the ratios of periodicities of 2.36 m: 0.95 m: 0.53 m is 4.5:1.8:1, correspond to the hierarchy of the frequencies of the orbital parameters of short eccentricity, obliquity, and precession. The hierarchy of cycles, with short alternations at a scale of 0.40 to 0.65 m, and longer periodicities of about 2–2.72, may correspond to the periodicities of precession and short eccentricity. The 10.50-m cycles, varying between 11.50 and 13.1 m and 8.01–9.97 m may represent the 405-ka component of long eccentricity. The periodicities shorter than 10.50 m are detected in the lower Aptian, yielding sedimentation rates of 2.5–1.9 cm/ka, that is in accordance with calculated sedimentation rates from ammonites (2.45 cm/ka) but differ from sedimentation rate calculated from foraminifera (5.42 cm/ka). The 11.50 and 13.1 m periodicities occur in the late Aptian, yielding a higher sedimentation rate of 3.1 cm/ka. That differs more from calculated sedimentation rates from biostratigraphy of 0.98 cm/ka (forams) and 1.04 cm/ka (ammonites). Applying the ammonite sedimentation rate to the 7.7–10 m periodicity results in durations of 314–408 ka.

5.1. Cyclostratigraphic interpretation

Peaks at 5.76, 4.38 and 4.00 m in the spectral analyses of this study (Fig. 5) could be the result of an interference between long- and short-components of eccentricity (Liebrand et al., 2017), or may represent the 200-ka eccentricity component (e.g., Hilgen et al., 2020). Another interpretation for this cyclicity may be the presence of obliquity amplitude modulation with a duration of 173 ka. An obliquity-related signal can be amplified by internal climate feedback of the carbon cycle under different geographic and climate conditions, as reported by Huang et al. (2021). Short eccentricity (~100 ka) is represented by periodicities of 2.72, 2.43 and 1.99 m in the record. Short eccentricity displays a loss of power in the MS record upsection (Figs. 5E-F). Obliquity is represented by periodicities of 1.11, 1.05, 0.96, 0.92, 0.87, 0.84 and 0.80 m, (Fig. 5). Precession is represented by periodicities of 0.65, 0.50, 0.47, 0.44, 0.43, 0.42 and 0.40 m (Fig. 5).

In the visual evaluation of the core and gamma ray and carbonate records, cycles of 0.80–1.1 m are observed, interpreted as obliquity cycles (Fig. 7). This variation in the length of this periodicity suggests a strong influence of variations in the tilt of Earth's axis on climate. The presence of obliquity fades in different intervals of the core, from 99.5 to 82 m depth, from 56 to 48 m, from 27.5 to 19 m, and from 9 m depth to the top of the core. This attenuation in the sedimentary imprint is associated with more variability in seasonality. Although the largest obliquity insolation amplitude effect is found at higher latitudes, some studies have found a significant obliquity signal in tropical latitudes (e.g., Park and Oglesby, 1991). During maximum obliquity, stronger monsoons can occur (Tuenter et al., 2005), as there is potential for atmospheric and oceanic currents to interplay between high and low latitudes, showing the interconnection of Earth's climatic system (Tuenter et al., 2003, 2005). The most significant influence of these remote mechanisms develops in the subtropics (20°–30°N) (Tuenter et al., 2003), where our study area was located.

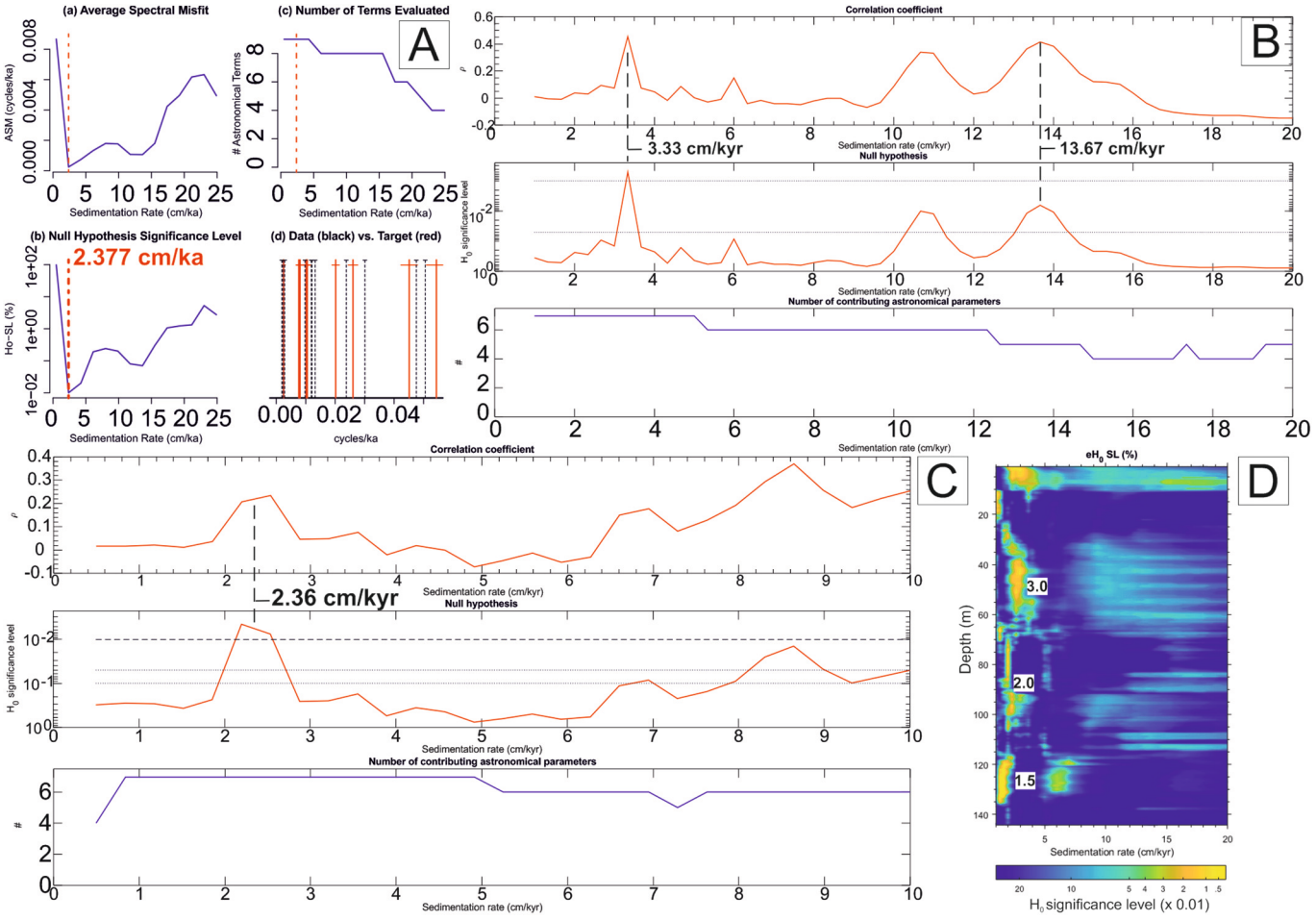

Fig. 6. A) ASM of the main frequencies detected in the gamma ray data over the complete record, performed in Astrochron. Frequencies analysed are above 99% confidence. Target orbital periodicities selected are components of eccentricity at 405-ka, 131-ka, 124-ka, 99-ka and 95-ka (in decreasing amplitude) and predicted orbital periods for obliquity (49.588-ka and 38.404-ka) and precession (22.156 and 18.392) for 118 Ma. The optimal sedimentation rate obtained using a range from 0.5 to 24.9 cm/ka (Table 1) for the Cau core is 2.377 cm/ka. The Astrochron script used is available in Appendix C. B) Correlation coefficient for the gamma ray record, with tested sedimentation rates range from 1 to 20 cm/ka. C) Correlation coefficient for the magnetic susceptibility record (from 110 m depth to the top), with tested sedimentation rates ranging from 0.5 to 10 cm/ka. D) eCOCO analysis of the gamma ray record, showing the null hypothesis (H_0) significance level. For both the COCO and eCOCO analyses, the number of Monte Carlo simulations is 2000. Parameters used are available in Appendix C.

Short-eccentricity cycles (between 1.7 and 2.7 m wide) are observed in most of the record, except for the interval from 128 to 118.4 m (Fig. 7), where the record is dominated by obliquity-paced cycles. This part of the record corresponds to the onset of OAE 1a, with variable sedimentation rates and an increase in clastic input from the continent through intensification of weathering (Castro et al., 2021; Martínez-Rodríguez et al., 2021). The influence of obliquity-paced cycles can be observed intermittently from 104 to 89 m. The carbonate record shows a stronger influence of obliquity than of precession, likely because of lacking carbonate levels. Although the western Tethys was under general warm conditions during the OAE 1a, the climate was unstable (Bottini and Erba, 2018). The intermittent presence of obliquity through OAE 1a may be indicative of changes in the latitudinal temperature gradient, allowing obliquity to affect the patterns in the exchange of energy over lower latitudes, in a similar way as described in Gubbio, at a very similar paleolatitude (25°N), in the Umbria-Marche basin (Sinnesael et al., 2016).

The presence of an obliquity imprint during the upper Aptian may be related to the long-lasting cooling in the western Tethys (O'Brien et al., 2017) and in the proto North-Atlantic (McAnena et al., 2013). A global cooling would imply that the latitudinal temperature differences become bigger and that the climate zones shift more toward the equator. In such a regime, the paleolocation of Cau likely came under a subtropical climatic regime (instead of purely tropical), in which remote obliquity mechanisms can have a larger effect (Tuenter et al., 2003).

This dominance of the obliquity periodicities over the precession cycles may have been affected by other factors. The probe used to measure gamma-ray is the QL40 GAM (see Martinez-Rodriguez, 2022), and the length of the sensor indicated by the manufacturer is 7.62 cm, considering an average lateral penetration adjacent to the hole of c. 20 cm, using a sample distance of 3 cm. This produces a smoothing effect, due to the overlapping area between consecutive measurements (Thibault and Perdiou, 2018), that is ≈20% of the cone of influence (Fig. 8), acting as a lowpass filter, which decreases the high frequencies. The sampling distance of $CaCO_3$ (10 cm), results in 4 to 6 points per precession cycle (thickness of 30–50 cm), generating an underestimation of the amplitude (Herbert, 2009). Finally, bioturbation mixes the sediment and decreases the high frequencies, especially if the sedimentation rate is lower than ~3 cm/ka (Hinnov, 2018; Martinez, 2018; Pisias, 1983). This may have partially affected the record, given the mean sedimentation rate of 2.37 cm/ka (Fig. 6A, C), but specially below 65 m depth (Fig. 6D), corresponding to the lower Aptian. Collectively, these biases may explain the higher power of in the obliquity band rather than in the precession band.

The paleolocation of Cau was within the humid and temperate subtropical paleoclimatic belt during the early Cretaceous. The dominance

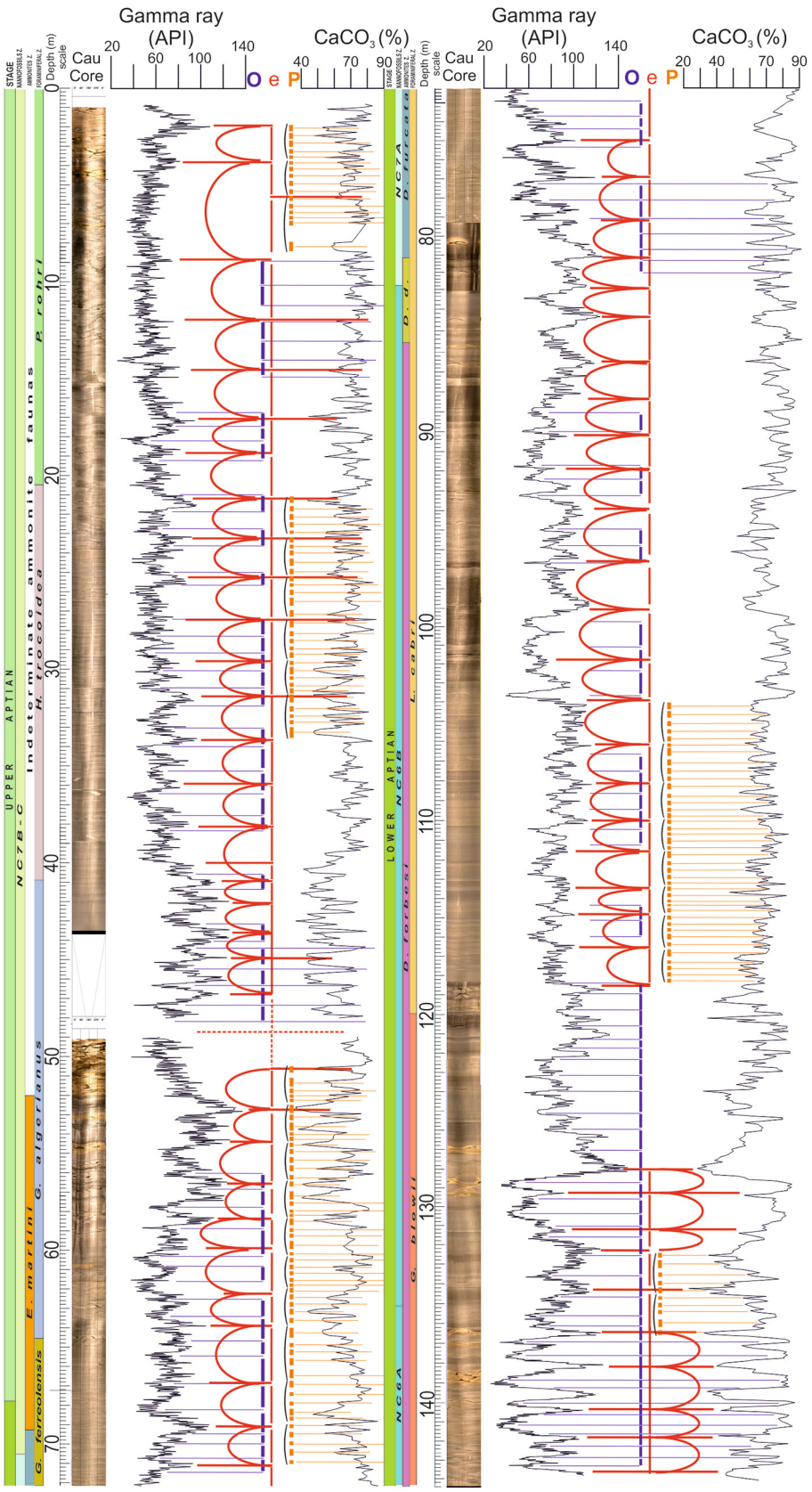

Fig. 7. High-resolution data from the Cau Core. On the left: depth scale in meters, flanked by the composite image from the Cau drill holes, the data of gamma ray (API units) and $CaCO_3$ content (%). Rhythmic banding patterns on different scales are represented by lines in different colours: orange bars indicate pairs of dark and light lithologies on a scale of 32–54 cm which are thought to represent the influence of precession; purple bars indicate variations on a scale of 61 cm to 1.1 m, thought to represent an obliquity influence; red arches delineate groupings of colour variations and oscillations in the data records on a scale of 1.7 to 2.7 m, and are

thought to represent the influence of short-eccentricity. (For interpretation of the references to colour in this figure legend, the reader is referred to the web version of this article.)

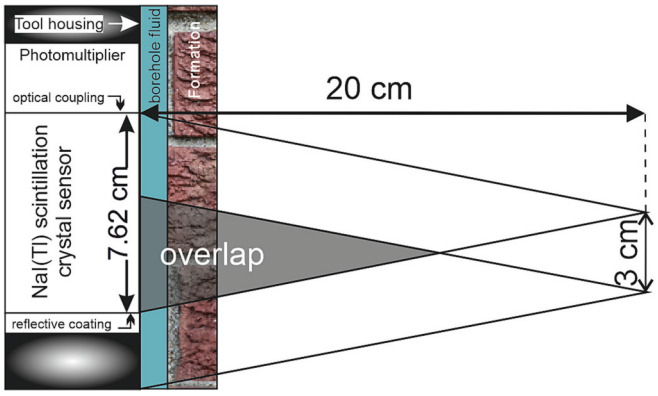

Fig. 8. Cone of influence for the gamma-ray probe used in this study, with a theoretical adjacent influence of 20 cm, in a wireline logging diagram showing an overlap of two consecutive measurements taken at 3 cm steps.

of temperate, humid subtropical and tropical savannah climate zones, representing a combined 70% of the total land area, would have resulted in higher Earth surface temperatures and reduced latitudinal gradients, thus, resulting in less climate variability (Burgener et al., 2023). Starting in the Aptian, a transition begins from a moderately-high CO_2 greenhouse world to a high CO_2 hothouse world in the Turonian, and as a consequence the Hardley cells begin to shrink during the Aptian (Hasegawa et al., 2012). This shrinking in Hardley cells and a southward shift of the equatorial humid belt from ~9° N in the Berriasian-Valanginian to 1° S in the Albian (Santos et al., 2022) influenced the climate of Cau in the long-term. Through the shrinking of the Hadley cell, Cau may have come under the influence of the Ferrel cell, with possible changes in oceanic circulation leading to changes in upwelling patterns and nutrient distribution. The southward shift of the Intertropical Convergence Zone (ITCZ) would result in decreased rainfall, thus leading to reduced riverine input of nutrients in the marine environment. Lower organic carbon production in the surface waters may result in decreased organic carbon burial rates. The long-term decreasing conditions in humid climate affecting marine productivity and organic carbon burial probably contributed to a less marked

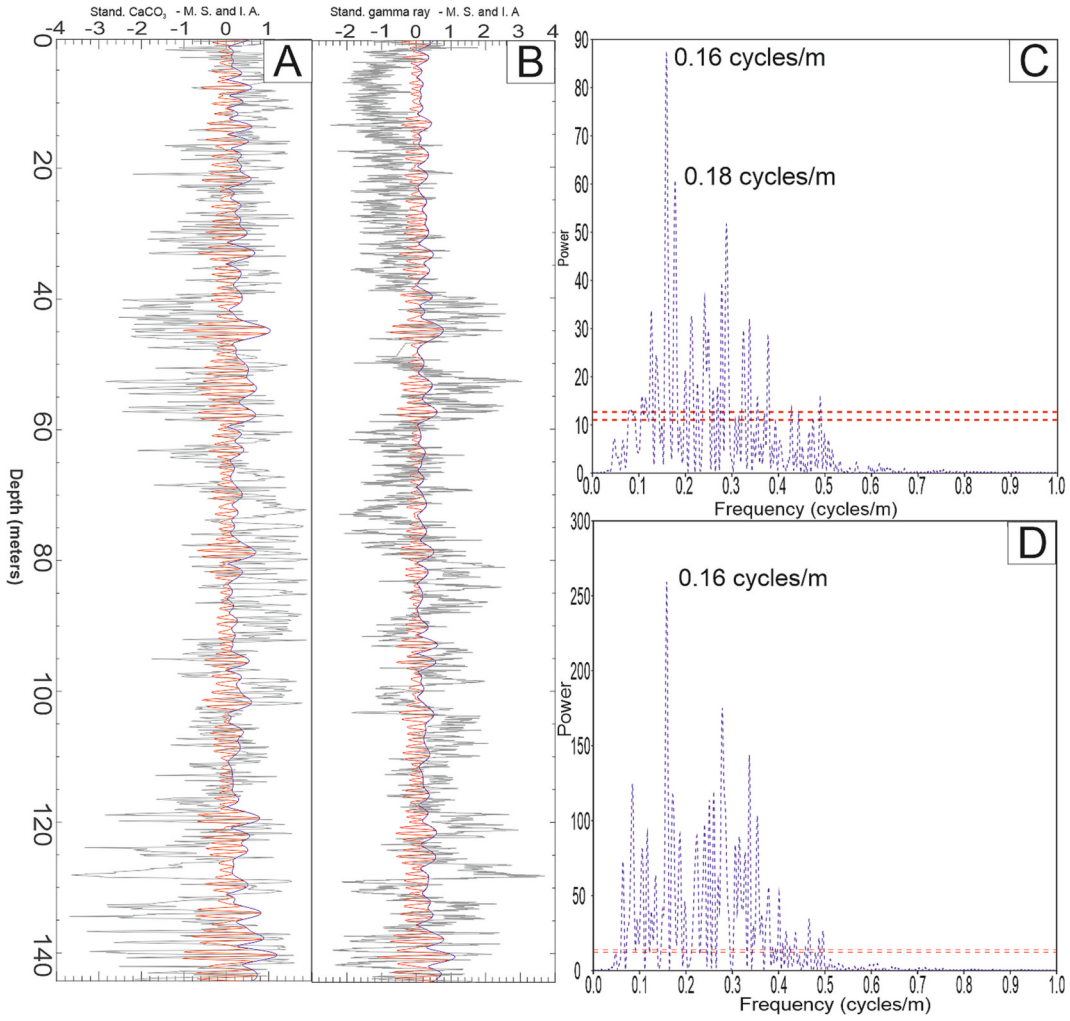

Fig. 9. Standardized $CaCO_3$ (A) and gamma ray (B) datasets, with Taner-Hilbert filters centred on a frequency of 1 cycle/m (flow 0.75 and fhigh 1.25, roll-off rate of 10^{24}). MS: modulated signal (in red), IA: instantaneous amplitude (envelope – in blue). C–D) Lomb-periodograms of the Taner-Hilbert filters of the $CaCO_3$ (C) and gamma ray (D) records. The most prominent frequencies are labelled in cycles/m. The upper and lower red dashed lines indicate a confidence levels of $p < 0.01$ and $p < 0.05$ in each periodogram, respectively. (For interpretation of the references to colour in this figure legend, the reader is referred to the web version of this article.)

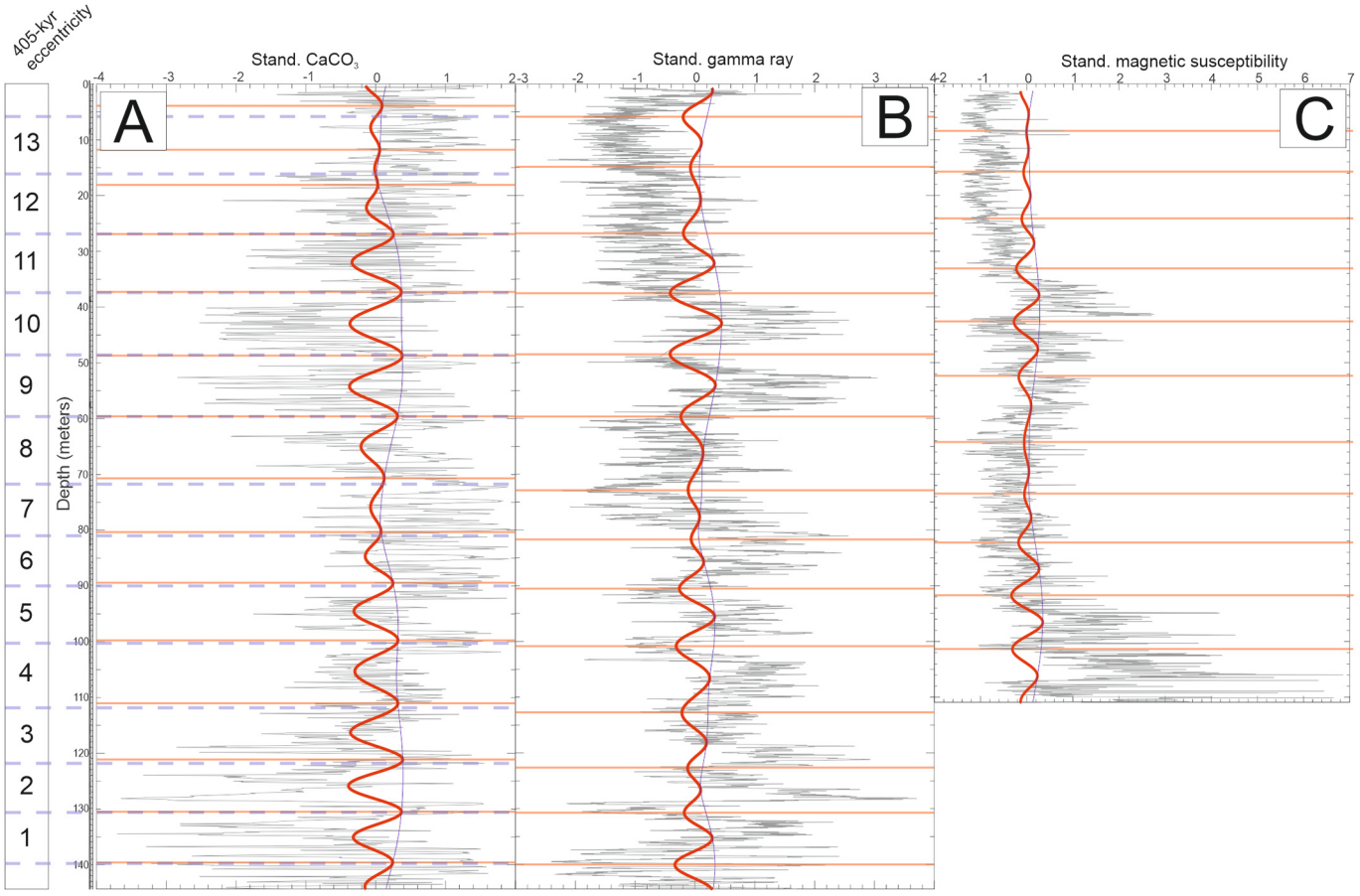

Fig. 10. Normalized $CaCO_3$ (A), gamma-ray (B) and MS (C) data (in grey), with Taner filters (red) centred on a frequency of 0.095 cycles/m, representing the 405-ka long eccentricity band. Tie-points for chronology represented by dashed purple lines. (For interpretation of the references to colour in this figure legend, the reader is referred to the web version of this article.)

modulation of the short eccentricity cycle in the upper Aptian record than in the lower Aptian (as shown in the MS record).

To test for a modulator of the obliquity, Taner filters have been calculated, for periodicities between 1.33 and 0.80 m, that correspond to obliquity in the $CaCO_3$ and gamma-ray records (Fig. 9A-B)A Hilbert transform was applied over the filter outputs, to calculate the instantaneous amplitude. The simple periodograms of the filters are displayed in Fig. 9 (C–D), and they show frequencies of 0.18 and 0.16 cycles/m as the highest peaks. This indicates that the periodicity of 5.76 m (frequency of 0.17 cycles/m), is possibly a long obliquity modulator, as previously described with a pacing of 173-ka in Huang et al. (2021).

5.2. Chronology

Although the La2010b solution (Laskar et al., 2011) is considered the best fit for geological data beyond 52 Ma (Westerhold et al., 2020), chaotic transitions are suspected in the upper Cretaceous (Ma et al., 2017) and a phase-relationship has not been established.

To calibrate the astronomical tuning for the complete record we have selected an anchor point at the boundary between the Ap11 and Ap12 segments (Fig. 2), from a revised chronology of the upper Aptian (Ait-Itto et al., 2023). This point coincides with the base of the "Faisceau Nolan" (Herrle et al., 2004), which is nine 405-ka eccentricity cycles below the Aptian-Albian boundary, dated itself as 113.2 ± 0.4 Ma, as proposed in the Geologic Time Scale 2020. Consequently, the base of the Ap11-Ap12 boundary is dated at 116.8 ± 0.4 Ma. This point (40.2 m depth) is located immediately under the bioevent of the last appearance of *G. algerianus* in this study (40.0 m depth) and correlates with a lithologic bundle linking the MS data from Charbonnier et al. (2023) to the C-isotope stratigraphy from Herrle et al. (2004).

Table 2
Tie-points for constructing the orbital age model. *Anchor point.

Depth (m)	Age (Ma)
26.9	116.3 ± 0.4
37.4	116.7 ± 0.4
*40.2	*116.8 ± 0.4
48.6	117.1 ± 0.4
59.6	117.5 ± 0.4
71.7	117.9 ± 0.4
81.3	118.3 ± 0.4
90.2	118.7 ± 0.4
100.4	119.1 ± 0.4
111.8	119.5 ± 0.4
121.8	119.9 ± 0.4
130.7	120.3 ± 0.4
139.8	120.7 ± 0.4

Taner-Hilbert bandpass filters with a lower and higher frequency cut of 0.076 cycles/m and 0.125 cycles/m (roll-off rate: 10^{12}) have been calculated for the $CaCO_3$, gamma ray and MS data (Fig. 10). Ages are assigned considering a constant duration of 405 ka between consecutive peaks in the filter of the 405-ka eccentricity cycle and data were interpolated linearly between tie points, thus assuming a constant sedimentation rate between two consecutive anchor points (Fig. 10) (Table 2). The error considered is the same as the floating age of the anchor point, 400-ka or ± 0.4 Ma. The tie points to anchor the orbitally calibrated age model have been selected picking the middle point between filter

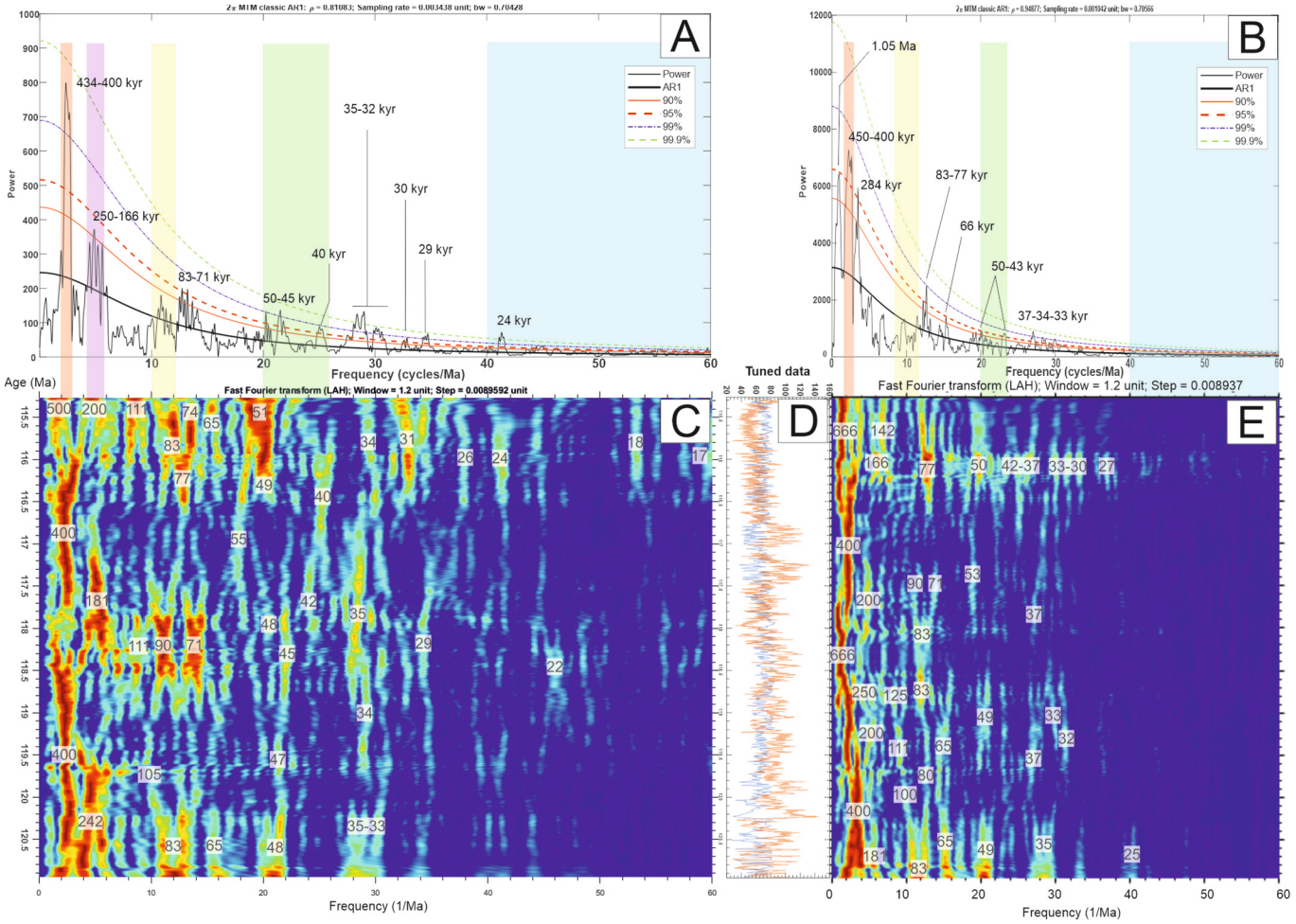

Fig. 11. Spectral analysis in the time domain, for the tuned data of $CaCO_3$ (A) and the gamma ray (B). The upper panels represent the 2π-Multi-Taper Method (MTM) spectra. Evolutive spectrograms with window size of 1.2 Ma are represented in the lower panels (C-E). D displays the tuned data of gamma ray (orange) and $CaCO_3$ (blue). Significant periods are labelled in Ma and ka. Colour bands represent the different ranges of astronomical parameters. The red band represents 405-ka eccentricity. Pink band: possible long obliquity modulation. Yellow band: 100-ka eccentricity. Green band: 40-ka obliquity. Blue band: 20-ka precession. (For interpretation of the references to colour in this figure legend, the reader is referred to the web version of this article.)

extremes of $CaCO_3$ and gamma ray, in order to distribute the error.

The investigated section spans from 115.28 Ma to 120.95 Ma (5.67 Ma), encompassing fourteen long eccentricity 405-ka cycles in total (Fig. 10). Spectral (MTM) and evolutionary spectral analyses by Fast Fourier transform (LAH), following Kodama and Hinnov (2014), have been conducted on the tuned $CaCO_3$ and gamma ray data (Fig. 11D). Evolutive harmonic analysis in the time domain (Fig. 11C) shows that spectral power is concentrated in a band centered around a 434–400 ka periodicity (frequency of 2.5 cycles/Ma – Fig. 11A) in the $CaCO_3$ record, which is a direct result of tuning to the periodicity of long eccentricity. In the gamma ray record, the spectral power in the long eccentricity band is less focused. The evolutionary analyses of both records display more power near the base and top of the core, from the base to 120.2 Ma, and from the top to 116.3 Ma, probably due to changes in sedimentation rate, and the introduction of additional incorrect frequencies due to zero padding introduced to cover the sliding window (1.2 Ma) at both ends. In the $CaCO_3$ harmonic analysis (Fig. 11C) there is more power in the interval from 117.7 to 118.7 Ma, and transfer of power from the long to the short eccentricity band (111–90-71 ka) is observed. The long obliquity modulation is better observed in the $CaCO_3$ record, both in the MTM (250–166 ka periodicities) and evolutive (242–200-181 ka periodicities) analyses (Figs. 11A-C). A series of prominent peaks above 99.9 and 99% confidence can be observed in the MTM spectra of both the $CaCO_3$ and gamma ray records (Fig. 11A-B) at 37–32 ka, possibly caused by an interference between obliquity and precession periodicities.

Table 3.1
Estimated age for the most prominent stratigraphic horizons present in this study.

Horizon	Depth (m)	Age (Ma)
NC - Nannoconid crisis	141.2	120.82
Ap2a-Ap2b (Onset CIE)	133.7	120.53
Ap2-Ap3 (OAE 1a onset)	125.4	120.20
Ap3-Ap4	119.5	119.97
Ap4-Ap5 (End CIE)	113.8	119.74
Ap5-Ap6	91.7	118.87
Ap6-Ap7 (OAE 1a end)	88.1	118.73
Ap7-Ap8	76.1	118.26
Ap8-Ap9	68.7	117.97
Ap9-Ap10	63.0	117.74
Ap10-Ap11	52.3	117.32
Ap11-Ap12	40.4	116.85
Ap12-Ap13	16.1	115.89
Ap13-Ap14	7.6	115.55

5.3. *Timescale, previous results, and implications*

Based on the high-resolution data from gamma ray, $CaCO_3$ and MS from the Cau Core, we propose a new astronomically calibrated

Table 3.2
Estimated timespan of bioevents from Leandro et al., (2022), and comparison with this study. *Top of the biostratigraphic zone.

Biostratigraphic zones	Age (Ma)* (Leandro et al., 2022)	Age* (Ma) (this study)	Timespan (Myr) (Leandro et al., 2022)	Timespan (Myr) (this study)
H. trocoidea	114.5	116.00	0.7	0.85
G. algerianus	115.2	116.85	2.2	0.89
G. ferreolensis	117.4	117.74	0.3	0.23
L. cabri	117.7	117.97	0.6	2.00
G. blowii		119.97		
Onset of NC	119.4	120.82		

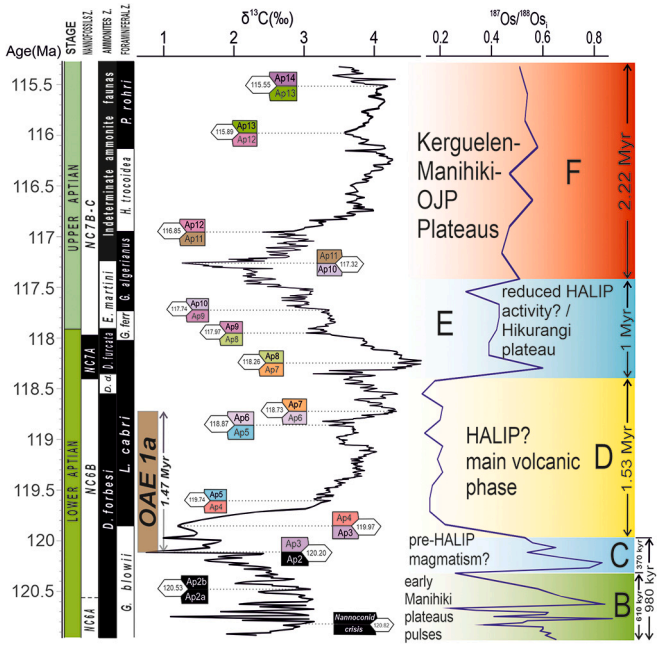

Fig. 12. Correlation of carbon (black line) and osmium (blue line) isotope values from the Cau section. The $\delta^{13}C$ record is from Castro et al. (2021), the Os_i record is from Martínez-Rodríguez et al. (2021), with available biostratigraphic data (left). The records of Cau are plotted against the age model derived from the independently established cyclostratigraphic interpretation of this section (this study). (For interpretation of the references to colour in this figure legend, the reader is referred to the web version of this article.)

chronology for the lower and middle Aptian of this intra-shelf basin site (Table 3.1). A comparison with other studied sections (Malinverno et al., 2010, the Cismon APTICORE in N Italy; Beil et al., 2020, La Bédoule in S France; Steuber et al., 2022, Abu Dhabi; Leandro et al., 2022, the Poggio le Guaine core; Charbonnier et al., 2023, in the Vocontian basin) for the duration of Aptian events is provided in Tables 3.2 and 3.4. The resultant chronology of this study is older than the duration calculated by Leandro et al. (2022). The onset of the NC at Cau (Fig. 12) is 1.42 Ma older than the age calculated at Poggio le Guaine (Table 3.2). Regarding the calculated timespan of the biozones, the timespan for the *G. ferreolensis* and *G. algerianus* biozones is similar, with 0.3 and 0.23 Ma, and with 0.7 and 0.85 Ma, respectively (Table 3.2), but the duration of the L. *cabri zone* is longer in this study (2.00 Ma) in comparison with the study from the Poggio le Guaine core (0.6 Ma) (Table 3.2). The biozone of *G. algerianus* is longer in the study from Leandro et al. (2022), with a time span of 2.2 Ma, in contrast to the 0.89 Ma calculated in this study (Table 3.2).

The differences found amongst Aptian records means that we are still far from reaching a unified astronomical timescale (ATS) for the Aptian stage. Independent relative age methods such as biostratigraphy and

Table 3.3
Estimated duration for the *Re*–Os isotope chemostratigraphy segments from Martínez-Rodríguez et al., (2021).

Re–Os isotope chemostratigraphy segments (Cau Core – from Martínez-Rodríguez et al., 2021)		Timespan (kyr)
B_2	Early HALIP?/Manihiki Plateaus pulses	310
C_1	HALIP? pre-massive magmatism	210
C_2		160
D_1		220
D_2	HALIP? main volcanic phase	570
D_3		740
E	Reduced HALIP? activity / Hikurangi plateau	1000

stratigraphic control (such as $\delta^{13}C$ chemostratigraphy), or absolute time methods (radio-isotopic dating), and differences in thickness/sedimentation rates between sections, as well as different hiatuses that could be present in the records, are a key factor when applying cyclostratigraphic studies, leading to different results. Regarding the different C-13 Aptian substages, the C3 stage (Ap notation in this study) calculated from the Cismon section is the shortest (46.7 ka), while the C3 stage calculated from the Vocontian Basin (Charbonnier et al., 2023) is the longest (485 ka). The duration of the C3 stage in this study is 230 ka, which is closer to the duration calculated from Steuber et al. (2022) at Abu Dhabi, of 104 ka (Table 3.4). The duration of segment C4 is similar in this study (230 ka) to the studies from Malinverno et al. (2010) (239 ka) and Charbonnier et al. (2023) (262 ka), whereas the C4 calculated from Abu Dhabi is shorter (40 ka) and the C4 duration calculated from La Bédoule is longer (388 ka, Table 3.4). The calculated timespan for the C5 segment is 360 ka longer in this study (870 ka) than in the study from Malinverno et al. (2010) (510 ka) (Table 3.4). In contrast, the C6 segment calculated from the Cismon section (349 ka) is 209 ka longer than in our calculations (140 ka) (Table 3.4). Segment C7 is much longer in the Cismon section, with a duration of 1590 ka, compared to this work (470 ka) (Table 3.4). Finally, the duration of OAE 1a calculated in this study (1470 ka, Fig. 12) agrees with the duration calculated from the Piobbico core (Huang et al., 2010), of 1400 ka. The duration estimates of OAE 1a from the Cismon and Poggio le Guaine cores are shorter with durations of 1110 and 920 ka respectively (Table 3.4). Recent data from the Vocontian Basin (Charbonnier et al., 2023) indicate an intermediate result of 1290 ka (Table 3.4).

Diverse time estimates can be related primarily to the thickness differences of the OAE 1a interval and its segments between sections, which are more marked in the C3 segment (Table 3.4). OAE 1a was defined at the Cismon section (Menegatti et al., 1998), with a reduced thickness, and a probable presence of hiatuses (Beil et al., 2020). Expanded sections of OAE 1a were studied later, from the Vocontian basin (e.g., Lorenzen et al., 2013; Charbonnier et al., 2023) and the Southern Iberian Paleomargin (de Gea et al., 2003; Castro et al., 2019, 2021), which provide a longer duration of the OAE 1a, doubtless due to a more complete record. Interestingly, the C6 segment has similar duration from the thin Cismon section (Malinverno et al., 2010) and the expanded Vocontian Basin (Beil et al., 2020) (Table 3.4). This can be related to the global context of extensional tectonics that occurred during the Early Aptian. Extensional pulses provoked abrupt paleogeographic changes in subsidence patterns, and therefore in sedimentation rates (e.g., Skelton et al., 2003; Martin-Chivelet et al., 2019).

Regarding the *Re*–Os chemostratigraphy from the Cau core (Martínez-Rodríguez et al., 2021), the durations of the detected oceanic magmatic phases have been calculated (Table 3.3, Fig. 12), in absence of any cosmic dust or meteoritic material source, although this cannot be totally discarded. Before analysing these results, a consideration must be made, relating to the main emplacement of the Ontong-Java Plateau (OJP). The emplacement is reported in literature to have occurred at ca. 123–121 Ma (Chambers et al., 2004), but a younger age for the emplacement of the Ontong-Java LIP has been proposed (Davidson et al., 2023), pointing to a connection of the OJP with OAE 1b, thus,

Table 3.4
Estimated duration for the most prominent stratigraphic features present in this study and comparison with studies from Li et al., (2008), Malinverno et al. (2010), Huang et al. (2010), Scott, (2016), Beil et al. (2020), Steuber et al. (2022), Leandro et al. (2022), and Charbonnier et al. (2023).

			Carbon isotope segment duration							
Reference	Location	Section/core	C3 (kyr)	C4 (kyr)	C5 (kyr)	C6 (kyr)	(C3-C6) OAE 1a (Myr)	C7 (kyr)	This study (kyr)	
This study	Prebetic zone	Cau	230	230	870	140	1.47	470	Ap2b	330
Charbonnier et al., 2023	Vocontian basin	composite	485	262	296	247	1.29		CIE (Ap2b-Ap3)	560
Leandro et al., 2022	Umbria Marche basin	Poggio le Guaine					0.92		Ap8	290
Steuber et al., 2022	Abu Dhabi	offshore well	104	40					Ap9	230
Beil et al., 2020	South Provence basin	La Bédoule	434	388	281	315	1.418		Ap10	420
Scott et al., 2016	Umbria Marche basin	Cismon	80	160	210	110	0.56	990	Ap11	470
		Rotter Sattel							Ap12	960
	Carbonate platform Mexico	Santa Rosa Canyon							Ap13	340
Moullade et al., 2015	South Provence basin	composite					1.157	1695		
Scott, 2014	various	composite					1.36			
Ogg and Huang, 2012	various	composite					1.5			
Huang et al., 2010	Umbria Marche basin	Piobbico					1.4			
Malinverno et al., 2010	Umbria Marche basin	Cismon	46.7	239	510	349	1.11 ± 0.11	1590		
Li et al., 2008	Carbonate platform Mexico	Santa Rosa Canyon	44	930		310	1.28			
	North Atlantic Ocean	DSDP Site 398					1–1.2			
	Umbria Marche basin	Cismon	27–41	330	570	330	1.27			

leaving OAE 1a without an identified volcanic source, except for the High Arctic Large Igneous Province (HALIP) (Dockman et al., 2018). Besides, the studied samples from the OJP belong to the top ~200 m from the surface of the plateau, whereas the top 8–9 km of the 35 km thick megastructure are considered the eruptive portion (Isse et al., 2021), so that, an older age for lower portions of the OJP cannot be discarded. Segment B_2, that corresponds to the early magmatic pulses from the Manihiki plateau, spans 310 ka (Table 3.3). Segment C, that may correspond with the pre-massive HALIP activity, spans 370 ka (Table 3, Fig. 12). The beginning of the main Os negative isotopic excursion is dated at 120.42 Ma, 120 ka (duration of C_2 segment) after the onset of OAE 1a. The possible main volcanic activity of the HALIP (segment D) is calculated to 1.53 Ma (from Table 3.3, Fig. 12). Segment E, corresponding to reduced activity from the HALIP/Hikurangi plateaus, presents a duration of 1 Ma (Table 3.3, Fig. 12).

Regarding OAE 1a, some consensus has been reached on the duration of the event (920 ka – 1.1 Ma – 1.29–1.40 Ma - 1.47 Ma), yet more variability is found when assessing the different parts of the event. E.g., four different calculated durations for the negative excursion (C3/Ap3 segment), 46.7, 104, 230 and 485 ka, yield a ten-fold difference between the Cismon section and the Vocontian Basin. At Cismon, the C3 segment is 0.26 m thick, whereas at La Bédoule, it is 6 m thick. This reveals that the character of the section, whether is condensed or expanded, can have an influence on the calculations. Leandro et al., (2022), based on their age estimate, suggest that the magmatic events from OJP and HALIP helped to trigger the oceanic anoxia recorded in the Selli Level (Polteau et al., 2016; Percival et al., 2021). On the one hand, the C3/Ap3 negative excursion requires more carbon than just the mantle carbon ($\delta^{13}C$ composition of −6‰, Gales et al., 2020), and the Hg-cycle perturbation is smaller than for the OJP (Percival et al., 2021). On the other hand, our study calculates a 115 ka delay between the onset of the OAE 1 and the main phase of non-radiogenic Os, pointing to the release of methane hydrates (Adloff et al., 2020) as a potential trigger of the C3/Ap3 segment. Methane hydrates are a suggested trigger for other OAEs, such as the Toarcian OAE (T-OAE), as they may explain negative $\delta^{13}C$ excursions. The cyclic $\delta^{13}C$ negative excursions found in the Cau core during the Ap2 segment also resemble those observed in the T-OAE (Kemp et al., 2005), pointing to an orbital control of the C-cycle influenced by short eccentricity. Finally, the broad positive $\delta^{13}C$ excursion (C4/Ap4 segment) also presents considerable divergences in calculated timespans, up to x10 times, e.g., from 40 ka (Stauber et al., 2022) to 388 ka (Beil et al., 2020), despite the C4 segment having a similar thickness in both sections (5.5 m thick in La Bédoule and 5.18 m thick in Abu Dhabi). Such different results underline the importance of the role that the selected cyclostratigraphic approach plays in these studies.

The phasing between maxima in $CaCO_3$ and minima in gamma-ray is roughly coincident from 20 m depth to the base of the core, so the reliability of the data can be considered as reasonably good from 20-depth until the base of the core, in the $CaCO_3$ and gamma ray data. However, the MS signal is out of phase from 0 m until 70 m depth, so the MS data seems to be less reliable. Nevertheless, extremes of the filters are more in phase from 80 m depth, with a maximum gap of ~2 m (between 112 and 122 m depth), so the accuracy of data in the interval of the OAE 1a (88 m to 125 m depth) may present less error.

6. Conclusions

The influence of obliquity and eccentricity-modulated precession is reflected in a hierarchy of cycles revealed by time series analysis of physical property and elemental data. However, this chronology has less confidence in the uppermost and lowermost part of the record, where the cyclicity is not clear. Although the uncertainty near the base causes difficulty for anchoring the record, the durations suggested by the cyclicity during the interval of OAE 1a can be considered robust. The intermittent presence of obliquity through the record may indicate cold snaps or transient cooling episodes in which climatic zones shift equatorward.

Data from this study provide ages of 120.95 Ma for the base of the Cau Core, and 115.28 Ma for the top of the Cau Core, with a time span of 5.67 Ma, which implies a mean sedimentation rate of 2.53 cm/ka. This result is more consistent with the sedimentation rate of 2.38 cm/ka obtained from the ASM (Fig. 6A) and the 2.36 cm/ka obtained from the MS COCO (Fig. 6C), than with the COCO/eCOCO results (peak of 3.33 cm/ka associated to a null hypthesis significance level lower than 0.001 – Fig. 6B). The investigated interval has permitted the construction of a 405-ka astronomically tuned age model. Based on the astronomical tuning, we have obtained a duration for OAE 1a of 1.47 Ma, an age for the NC of 120.82 Ma, and of 120.20 Ma for the onset of OAE 1a. The calculated age for the onset of the main non-radiogenic phase of Os_i isotopes is 120.32 Ma, occurring 120 ka after the onset of OAE 1a. The duration of the main non-radiogenic phase of the Os-isotopes is calculated as 1.53 Ma. As evident from different authors, there are still

substantial differences in the calculated ages and durations for the different intervals and horizons from the Aptian stage and for the different phases within OAE 1a. Furthermore, the danger of linking the OJP LIP with OAE 1a can lead to incorrect conclusions, pointing to a need to reevaluate causal relationships between igneous and sedimentary records, as in the lack of cosmogenic sources, to better understand major biosphere perturbations such as OAEs and LIPs.

CRediT authorship contribution statement

Rafael Martínez-Rodríguez: Conceptualization, Data curation, Formal analysis, Investigation, Methodology, Software, Supervision, Validation, Visualization, Writing – original draft, Writing – review & editing. **Sietske J. Batenburg:** Investigation, Methodology, Software, Supervision, Writing – review & editing. **José M. Castro:** Project administration, Resources, Supervision, Writing – review & editing. **Ginés A. de Gea:** Writing – review & editing, Supervision. **Luis M. Nieto:** Supervision, Writing – review & editing. **Pedro A. Ruiz-Ortiz:** Funding acquisition, Project administration, Writing – review & editing. **Stuart Robinson:** Funding acquisition, Writing – review & editing.

Declaration of competing interest

The authors declare that they have no known competing financial interests or personal relationships that could have appeared to influence the work reported in this paper.

Data availability

The data used and generated is attached in the file step. (as Appendix A)

Acknowledgements

We thank the anonymous reviewers for their careful reading of our manuscript and their many insightful comments and suggestions. The authors are very grateful for the constructive review of M. Martinez, which led to improvements of the final version of the manuscript. This work is the result of a research visit to the University of Oxford by the first author and is a contribution to his PhD thesis within the research group RNM-200 "Basin Analysis and Environmental Geology". Professors J. M. Molina, M. L. Quijano and M. Reolid, members of the "Cau Core Project", contributed with the sampling and analysis of the core. Drs. D. Gallego-Torres, J. M. Ramírez, C. López-Rodríguez and M. Rodrigo Gámiz participated in the sampling and description of the cores. Laboratory technicians I. Sanchis, J. Lechuga, A. Molero and A. Fernández are acknowledged for their help in sampling and processing samples from the core. Funding for this study was provided by project CGL2014-55274-P of the Spanish Ministry of Science and Technology, project 06.17.02.80.P1 of the University of Jaén and FEDER, a PhD-student scholarship and a stage grant from the University of Jaén (Spain) given to RMR. In loving memory of Professor Roque Aguado Merlo.

Supplementary data

Supplementary data to this article can be found online at https://doi.org/10.1016/j.gloplacha.2024.104361.

References

Adloff, M., Greene, S.E., Parkinson, I.J., Naafs, B.D.A., Preston, W., Ridgwell, A., Lunt, D. J., Castro Jiménez, J.M., Monteiro, F.M., 2020. Unravelling the sources of carbon emissions at the onset of Oceanic Anoxic Event (OAE) 1a. Earth Planet. Sci. Lett. 530, 115947 https://doi.org/10.1016/j.epsl.2019.115947.

Ait-Itto, F.-Z., Martinez, M., Deconinck, J.-F., Bodin, S., 2023. Astronomical calibration of the OAE1b from the Col de Pré-Guittard section (Aptian–Albian), Vocontian Basin, France. Cretaceous Research 150, 105618. https://doi.org/10.1016/j.cretres.2023.105618.

Ando, A., Kaiho, K., Kawahata, H., Kakegawa, T., 2008. Timing and magnitude of early Aptian extreme warming: Unraveling primary δ18O variation in indurated pelagic carbonates at Deep Sea Drilling Project Site 463, Central Pacific Ocean. Palaeogeography, Palaeoclimatology, Palaeoecology 260 (3–4), 463–476. https://doi.org/10.1016/j.palaeo.2007.12.007.

Ando, T., Sawada, K., Okano, K., Takashima, R., Nishi, H., 2017. Marine primary producer community during the mid-cretaceous oceanic anoxic events (OAEs) 1a, 1b and 1d in the Vocontian Basin (SE France) evaluated from triaromatic steroids in sediments. Org. Geochem. 106, 13–24. https://doi.org/10.1016/j.orggeochem.2017.02.002.

Archer, D., 2011. The Global Carbon Cycle: Vol. In: Princeton Primers, 2010th ed. Princeton University Press https://press.princeton.edu/books/paperback/9780691144146/the-global-carbon-cycle.

Arthur, M.A., Jenkyns, H.C., Brumsack, H.J., Schlanger, S.O., 1990. In: Ginsburg, R.N., Beaudoin, B. (Eds.), Cretaceous Resources, Events and Rhythms. Springer, Netherlands. https://doi.org/10.1007/978-94-015-6861-6.

Batenburg, S.J., De Vleeschouwer, D., Sprovieri, M., Hilgen, F.J., Gale, A.S., Singer, B.S., Koeberl, C., Coccioni, R., Claeys, P., Montanari, A., 2016. Orbital control on the timing of oceanic anoxia in the late cretaceous. Climate of the Past 12 (10), 1995–2009. https://doi.org/10.5194/cp-12-1995-2016.

Beil, S., Kuhnt, W., Holbourn, A., Scholz, F., Oxmann, J., Wallmann, K., Lorenzen, J., Aquit, M., Hassane Chellai, E., 2020. Cretaceous oceanic anoxic events prolonged by phosphorus cycle feedbacks. Clim. Past 16 (2), 757–782. https://doi.org/10.5194/CP-16-757-2020.

Berger, A., Loutre, M.F., Laskar, J., 1992. Stability of the Astronomical Frequencies over the Earth's history for Paleoclimate Studies. Science 255 (5044), 560–566. https://doi.org/10.1126/SCIENCE.255.5044.560.

Berner, R.A., 2004. The Phanerozoic Carbon Cycle: CO2 and O2. The Phanerozoic Carbon Cycle. https://doi.org/10.1093/OSO/9780195173338.001.0001.

Bodin, S., Meissner, P., Janssen, N.M.M., Steuber, T., Mutterlose, J., 2015. Large igneous provinces and organic carbon burial: Controls on global temperature and continental weathering during the early cretaceous. Global Planet. Change 133, 238–253. https://doi.org/10.1016/J.GLOPLACHA.2015.09.001.

Bottini, C., Erba, E., 2018. Mid-cretaceous paleoenvironmental changes in the western Tethys. Climate of the Past 14 (8), 1147–1163. https://doi.org/10.5194/CP-14-1147-2018.

Bralower, T., CoBabe, E., Clement, B., Sliter, W., Osburn, C., Longoria, J., 1999. The record of global change in mid-cretaceous (Barremian-Albian) sections from the Sierra Madre, Northeastern Mexico. *The*. J. Foraminifer. Res. 29.

Bréhéret, J.-G., 1994. The Mid-cretaceous Organic-Rich Sediments from the Vocontian Zone of the French Southeast Basin. Hydrocarbon and Petroleum Geology of France 295–320. https://doi.org/10.1007/978-3-642-78849-9_21.

Bréhéret, J.-G., 1995. L'Aptien et l'albien de la fosse Vocontienne (des bordures au bassin) : évolution de la sédimentation et enseignements sur les évènements anoxiques. https://theses.hal.science/tel-00805488.

Burgener, L., Hyland, E., Reich, B.J., Scotese, C., 2023. Cretaceous climates: Mapping paleo-Köppen climatic zones using a Bayesian statistical analysis of lithologic, paleontologic, and geochemical proxies. Palaeogeography, Palaeoclimatology, Palaeoecology 613, 111373. https://doi.org/10.1016/j.palaeo.2022.111373.

Caillaud, A., Quijada, M., Huet, B., Reynaud, J.Y., Riboulleau, A., Bout-Roumazeilles, V., Baudin, F., Chappaz, A., Adatte, T., Ferry, J.N., Tribovillard, N., 2020. Turbidite-induced re-oxygenation episodes of the sediment-water interface in a diverticulum of the Tethys Ocean during the Oceanic Anoxic Event 1a: the French Vocontian Basin. The Depositional Record 6 (2), 352–382. https://doi.org/10.1002/DEP2.102.

Caillaud, A., Quijada, M., Hlohowskyj, S.R., Chappaz, A., Bout-Roumazeilles, V., Reynaud, J.Y., Riboulleau, A., Baudin, F., Adatte, T., Ferry, J.N., Tribovillard, N., 2022. Assessing controls on organic matter enrichments in hemipelagic marls of the Aptian-lower Albian Blue Marls of the Vocontian Basin (France): an unexpected variability observed from multiple "organic-rich" levels. BSGF - Earth Sciences Bulletin 193 (3). https://doi.org/10.1051/BSGF/2022001.

Castro, J.M., de Gea, G.A., Ruiz-Ortiz, P.A., Nieto, L.M., 2008. Development of carbonate platforms on an extensional (rifted) margin: the Valanginian–Albian record of the Prebetic of Alicante (SE Spain). Cretaceous Research 29 (5–6), 848–860. https://doi.org/10.1016/J.CRETRES.2008.05.012.

Castro, J.M., de Gea, G.A., Quijano, M.L., Aguado, R., Froehner, S., Naafs, B.D.A., Pancost, R.D., 2019. Complex and protracted environmental and ecological perturbations during OAE 1a - evidence from an expanded pelagic section from South Spain (Western Tethys). Global Planet. Change 183, 103030. https://doi.org/10.1016/J.GLOPLACHA.2019.103030.

Castro, J.M., Ruiz-Ortiz, P.A., de Gea, G.A., Aguado, R., Jarvis, I., Weissert, H., Molina, J. M., Nieto, L.M., Pancost, R.D., Quijano, M.L., Reolid, M., Skelton, P.W., López-Rodríguez, C., Martínez-Rodríguez, R., 2021. High-Resolution C-Isotope, TOC and Biostratigraphic Records of OAE 1a (Aptian) from an Expanded Hemipelagic Cored Succession, Western Tethys: a New Stratigraphic Reference for Global Correlation and Paleoenvironmental Reconstruction. Paleoceanography and Paleoclimatology 36 (3). https://doi.org/10.1029/2020PA004004 e2020PA004004.

Chambers, L.M., Pringle, M.S., Fitton, J.G., 2004. Phreatomagmatic eruptions on the Ontong Java Plateau: an Aptian 40Ar/39Ar age for volcaniclastic rocks at ODP Site 1184. Geol. Soc. Spec. Pub. 229, 325–331. https://doi.org/10.1144/GSL.SP.2004.229.01.18.

Charbonnier, G., Boulila, S., Spangenberg, J.E., Vermeulen, J., Galbrun, B., 2023. Astrochronology of the Aptian stage and evidence for the chaotic orbital motion of Mercury. Earth Planet. Sci. Lett. 610, 118104 https://doi.org/10.1016/J.EPSL.2023.118104.

Cleveland, W.S., 1979. Robust locally Weighted Regression and Smoothing Scatterplots. J. Am. Stat. Assoc. 74 (368), 829. https://doi.org/10.2307/2286407.
Cohen, K.M., Finney, S.C., Gibbard, P.L., Fan, J.X., 2013. The ICS international chronostratigraphic chart. Episodes 36 (3), 199–204. https://doi.org/10.18814/EPIIUGS/2013/V36I3/002.
Davidson, P.C., Koppers, A.A.P., Sano, T., Hanyu, T., 2023. A younger and protracted emplacement of the Ontong Java Plateau. Science 380 (6650), 1185–1188. https://doi.org/10.1126/science.ade8666.
De Gea, G.A., Castro, J.M., Aguado, R., Ruiz-Ortiz, P.A., Company, M., 2003. Lower Aptian carbon isotope stratigraphy from a distal carbonate shelf setting: the Cau section, Prebetic zone, SE Spain. Palaeogeography, Palaeoclimatology, Palaeoecology 200 (1–4), 207–219. https://doi.org/10.1016/S0031-0182(03)00451-6.
Dockman, D.M., Pearson, D.G., Heaman, L.M., Gibson, S.A., Sarkar, C., 2018. Timing and origin of magmatism in the Sverdrup Basin, Northern Canada—Implications for lithospheric evolution in the High Arctic large Igneous Province (HALIP). Tectonophysics 742–743, 50–65. https://doi.org/10.1016/J.TECTO.2018.05.010.
Elkhazri, A., Abdallah, H., Razgallah, S., Moullade, M., Kuhnt, W., 2013. Carbon-isotope and microfaunal stratigraphy bounding the lower Aptian Oceanic Anoxic Event 1a in northeastern Tunisia. Cretaceous Research 39, 133–148. https://doi.org/10.1016/J.CRETRES.2012.05.011.
Erba, E., Channell, J.E.T., Claps, M., Jones, C.E., Larson, R.L., Opdyke, B., Silva, I.P., Riva, A., Salvini, G., Torricelli, S., 1999. Integrated stratigraphy of the Cismon Apticore (southern Alps, Italy); a reference section for the Barremian-Aptian interval at low latitudes. Journal of Foraminiferal Research 29, 371–391. https://api.semanticscholar.org/CorpusID:131000328.
Erba, E., Duncan, R.A., Bottini, C., Tiraboschi, D., Weissert, H., Jenkyns, H.C., Malinverno, A., 2015. Environmental consequences of Ontong Java Plateau and Kerguelen Plateau volcanism. Special Paper of the Geological Society of America 511, 271–303. https://doi.org/10.1130/2015.2511(15).
Ferry, S., 2017. Summary on Mesozoic Carbonate Deposits of the Vocontian Trough (Subalpine Chains, SE France). Carnets de Géologie / Notebooks on Geology.
Föllmi, K.B., 2012. Early Cretaceous life, climate and anoxia. Cretaceous Res. 35, 230–257. https://doi.org/10.1016/J.CRETRES.2011.12.005.
Friedrich, O., Reichelt, K., Herrle, J.O., Lehmann, J., Pross, J., Hemleben, C., 2003. Formation of the late Aptian Niveau Fallot black shales in the Vocontian Basin (SE France): evidence from foraminifera, palynomorphs, and stable isotopes. Mar. Micropaleontol. 49 (1–2), 65–85. https://doi.org/10.1016/S0377-8398(03)00029-X.
Friedrich, O., Norris, R.D., Erbacher, J., 2012. Evolution of middle to late cretaceous oceans—a 55 m.y. record of Earth's temperature and carbon cycle. Geology 40 (2), 107–110. https://doi.org/10.1130/G32701.1.
Friès, G., Parize, O., 2003. Anatomy of ancient passive margin slope systems: Aptian gravity-driven deposition on the Vocontian palaeomargin, western Alps, south-East France. Sedimentology 50 (6), 1231–1270. https://doi.org/10.1111/J.1365-3091.2003.00601.X.
Gradstein, F.M., Ogg, J.G., Schmitz, M.D., Ogg, G.M., 2020. Geologic Time Scale 2020. Geologic Time Scale 2020, 1–1357. https://doi.org/10.1016/C2020-1-02369-3.
Gröcke, D.R., Hesselbo, S.P., Jenkyns, H.C., 1999. Carbon-isotope composition of lower cretaceous fossil wood: Ocean-atmosphere chemistry and relation to sea-level change. Geology 27 (2), 155–158. https://doi.org/10.1130/0091-7613(1999)027<0155:CICOLC>2.3.CO;2.
Hasegawa, H., Tada, R., Jiang, X., Suganuma, Y., Imsamut, S., Charusiri, P., Ichinnorov, N., Khand, Y., 2012. Drastic shrinking of the Hadley circulation during the mid-cretaceous Supergreenhouse. Climate of the Past 8 (4), 1323–1337. https://doi.org/10.5194/CP-8-1323-2012.
Heimhofer, U., Hochuli, P.A., Herrle, J.O., Andersen, N., Weissert, H., 2004. Absence of major vegetation and palaeoatmospheric pCO2 changes associated with oceanic anoxic event 1a (early Aptian, SE France). Earth Planet. Sci. Lett. 223 (3–4), 303–318. https://doi.org/10.1016/J.EPSL.2004.04.037.
Heimhofer, U., Hochuli, P.A., Herrle, J.O., Weissert, H., 2006. Contrasting origins of early cretaceous black shales in the Vocontian basin: evidence from palynological and calcareous nannofossil records. Palaeogeography, Palaeoclimatology, Palaeoecology 235 (1–3), 93–109. https://doi.org/10.1016/J.PALAEO.2005.09.025.
Heldt, M., Bachmann, M., Lehmann, J., 2008. Microfacies, biostratigraphy, and geochemistry of the hemipelagic Barremian–Aptian in north-central Tunisia: Influence of the OAE 1a on the southern Tethys margin. Palaeogeography, Palaeoclimatology, Palaeoecology 261 (3–4), 246–260. https://doi.org/10.1016/J.PALAEO.2008.01.013.
Herbert, T.D., 2009. Reading Orbital Signals Distorted by Sedimentation: Models and examples. International Association of Sedimentologists Series 483–507. https://doi.org/10.1002/9781444304039.CH29.
Herrle, J.O., Pross, J., Friedrich, O., Kößler, P., Hemleben, C., 2003. Forcing mechanisms for mid-cretaceous black shale formation: evidence from the Upper Aptian and lower Albian of the Vocontian Basin (SE France). Palaeogeography, Palaeoclimatology, Palaeoecology 190, 399–426. https://doi.org/10.1016/S0031-0182(02)00616-8.
Herrle, J.O., Kößler, P., Friedrich, O., Erlenkeuser, H., Hemleben, C., 2004. High-resolution carbon isotope records of the Aptian to lower Albian from SE France and the Mazagan Plateau (DSDP Site 545): a stratigraphic tool for paleoceanographic and paleobiologic reconstruction. Earth Planet. Sci. Lett. 218 (1–2), 149–161. https://doi.org/10.1016/S0012-821X(03)00646-0.
Herrle, J.O., Kössler, P., Bollmann, J., 2010. Palaeoceanographic differences of early late Aptian black shale events in the Vocontian Basin (SE France). Palaeogeography, Palaeoclimatology, Palaeoecology 297 (2), 367–376. https://doi.org/10.1016/J.PALAEO.2010.08.015.
Hilgen, F., Zeeden, C., Laskar, J., 2020. Paleoclimate records reveal elusive ~200-ka eccentricity cycle for the first time. Global Planet. Change 194, 103296. https://doi.org/10.1016/J.GLOPLACHA.2020.103296.
Hinnov, L.A., 2018. Cyclostratigraphy and Astrochronology in 2018, 3, pp. 1–80. https://doi.org/10.1016/BS.SATS.2018.08.004.
Hu, X., Zhao, K., Yilmaz, I.O., Li, Y., 2012. Stratigraphic transition and palaeoenvironmental changes from the Aptian oceanic anoxic event 1a (OAE1a) to the oceanic red bed 1 (ORB1) in the Yenicesihlar section, Central Turkey. Cretaceous Research 38, 40–51. https://doi.org/10.1016/J.CRETRES.2012.01.007.
Huang, C., Hinnov, L., Fischer, A.G., Grippo, A., Herbert, T., 2010. Astronomical tuning of the Aptian Stage from Italian reference sections. Geology 38 (10), 899–902. https://doi.org/10.1130/G31177.1.
Huang, H., Gao, Y., Ma, C., Jones, M.M., Zeeden, C., Ibarra, D.E., Wu, H., Wang, C., 2021. Organic carbon burial is paced by a ~173-ka obliquity cycle in the middle to high latitudes. Sci. Adv. 7 (28), 9489–9498. https://doi.org/10.1126/SCIADV.ABF9489/SUPPL_FILE/ABF9489_TABLE_S2.CSV.
Husson, D., 2014. MathWorks File Exchange: RedNoise_ConfidenceLevels. Http://Www.Mathworks.Com/Matlabcentral/Fileexchange/45539-Rednoise-Confidencelevels/Content/RedNoise_ConfidenceLevels/RedConf.m.
Isse, T., Suetsugu, D., Ishikawa, A., et al., 2021. Seismic evidence for a thermochemical mantle plume underplating the lithosphere of the Ontong Java Plateau. Commun Earth Environ 2, 98. https://doi.org/10.1038/s43247-021-00169-9.
Jenkyns, H.C., 2018. Transient cooling episodes during cretaceous Oceanic Anoxic events with special reference to OAE 1a (early Aptian). Philos. Trans. R. Soc. A Math. Phys. Eng. Sci. 376 (2130) https://doi.org/10.1098/RSTA.2017.0073.
Kodama, K.P., Hinnov, L.A., 2014. Rock magnetic cyclostratigraphy. Rock Magnetic Cyclostratigraphy 1–165. https://doi.org/10.1002/9781118561294, 9781118561287.
Kuhnt, W., Holbourn, A., Moullade, M., 2011. Transient global cooling at the onset of early Aptian oceanic anoxic event (OAE) 1a. Geology 39 (4), 323–326. https://doi.org/10.1130/G31554.1.
Laskar, J., Fienga, A., Gastineau, M., Manche, H., 2011. La2010: a new orbital solution for the long-term motion of the Earth. Astron. Astrophys. 532, A89. https://doi.org/10.1051/0004-6361/201116836.
Laskar, J., Robutel, P., Joutel, F., Gastineau, M., Correia, A.C.M., Levrard, B., 2004. A long-term numerical solution for the insolation quantities of the Earth. Astron. Astrophys. 428 (1), 261–285. https://doi.org/10.1051/0004-6361:20041335.
Leandro, C.G., Savian, J.F., Kochhann, M.V.L., Franco, D.R., Coccioni, R., Frontalini, F., Gardin, S., Jovane, L., Figueiredo, M., Tedeschi, L.R., Janikian, L., Almeida, R.P., Trindade, R.I.F., 2022. Astronomical tuning of the Aptian stage and its implications for age recalibrations and paleoclimatic events. Nature Communications 2022 13:1 13 (1), 1–12. https://doi.org/10.1038/s41467-022-30075-3.
Li, Y.X., Bralower, T.J., Montañez, I.P., Osleger, D.A., Arthur, M.A., Bice, D.M., Herbert, T.D., Erba, E., Premoli Silva, I., 2008. Toward an orbital chronology for the early Aptian Oceanic Anoxic Event (OAE1a, ~ 120 Ma). Earth Planet. Sci. Lett. 271 (1–4), 88–100. https://doi.org/10.1016/J.EPSL.2008.03.055.
Li, M., Hinnov, L., Kump, L., 2019. Acycle: Time-series analysis software for paleoclimate research and education. Comput. Geosci. 127, 12–22. https://doi.org/10.1016/J.CAGEO.2019.02.011.
Liebrand, D., De Bakker, A.T.M., Beddow, H.M., Wilson, P.A., Bohaty, S.M., Ruessink, G., Pälike, H., Batenburg, S.J., Hilgen, F.J., Hodell, D.A., Huck, C.E., Kroon, D., Raffi, I., Saes, M.J.M., Van Dijk, A.E., Lourens, L.J., 2017. Evolution of the early Antarctic ice ages. Proc. Natl. Acad. Sci. U. S. A. 114 (15), 3867–3872. https://doi.org/10.1073/PNAS.1615440114/SUPPL_FILE/PNAS.201615440SI.PDF.
Lorenzen, J., Kuhnt, W., Holbourn, A., Flögel, S., Moullade, M., Tronchetti, G., 2013. A new sediment core from the Bedoulian (lower Aptian) stratotype at Roquefort-La Bédoule, SE France. Cretac. Res. 39, 6–16. https://doi.org/10.1016/J.CRETRES.2012.03.019.
Ma, C., Meyers, S.R., Sageman, B.B., 2017. Theory of chaotic orbital variations confirmed by cretaceous geological evidence. Nature 542 (7642), 468–470. https://doi.org/10.1038/nature21402.
Malinverno, A., Erba, E., Herbert, T.D., 2010. Orbital tuning as an inverse problem: Chronology of the early Aptian oceanic anoxic event 1a (Selli Level) in the Cismon APTICORE. Paleoceanography 25 (2), 2203. https://doi.org/10.1029/2009PA001769.
Martín-Chivelet, J., López-Gómez, J., Aguado, R., Arias, C., Arribas, J., Eugenia Arribas, M., Aurell, M., Bádenas, B., Isabel Benito, M., Bover-Arnal, T., Casas-Sainz, A., Manuel Castro, J., Coruña, F., de Gea, G.A., Fornós, J.J., Fregenal-Martínez, M., García-Senz, J., Garófano, D., Gelabert, B., et al., 2019. The Late Jurassic–Early Cretaceous Rifting. Regional Geology Reviews 169–249. https://doi.org/10.1007/978-3-030-11295-0_5.
Martinez, M., 2018. Mechanisms of Preservation of the Eccentricity and Longer-term Milankovitch Cycles in Detrital Supply and Carbonate Production in Hemipelagic Marl-Limestone Alternations, pp. 189–218. https://doi.org/10.1016/BS.SATS.2018.08.002.
Martinez, M., Deconinck, J.F., Pellenard, P., Riquier, L., Company, M., Reboulet, S., Moiroud, M., 2015. Astrochronology of the Valanginian–Hauterivian stages (Early Cretaceous): Chronological relationships between the Paraná–Etendeka large igneous province and the Weissert and the Faraoni events. Global Planet. Change 131, 158–173. https://doi.org/10.1016/J.GLOPLACHA.2015.06.001.
Martinez, M., Aguado, R., Company, M., Sandoval, J., O'Dogherty, L., 2020. Integrated astrochronology of the Barremian Stage (early cretaceous) and its biostratigraphic subdivisions. Global Planet. Change 195, 103368. https://doi.org/10.1016/J.GLOPLACHA.2020.103368.
Martinez, M., Aguirre-Urreta, B., Dera, G., Lescano, M., Omarini, J., Tunik, M., O'Dogherty, L., Aguado, R., Company, M., Bodin, S., 2023. Synchrony of carbon

cycle fluctuations, volcanism and orbital forcing during the early cretaceous. Earth-Science Reviews 239, 104356. https://doi.org/10.1016/j.earscirev.2023.104356.
Zhang, Y., Ogg, J.G., Minguez, D., Hounslow, M.W., Olaussen, S., Gradstein, F.M., Esmeray-Senlet, S., 2021. Magnetostratigraphy of U-Pb–dated boreholes in Svalbard, Norway, implies that magnetochron M0r (a proposed Barremian-Aptian boundary marker) begins at 121.2±0.4 Ma. Geology 49 (6), 733–737. https://doi.org/10.1130/G48591.1.
Martinez-Rodriguez, R., 2022. Record of Environmental Changes during the Aptian of the Prebetic (Betic External Zones). Characterization, Correlation and Control Factors (Unpublished doctoral dissertation). University of Jaén, Jaén.
Martínez-Rodríguez, R., Castro, J.M., De, G.A., Guillén, G., Nieto, L.M., Reolid, M., Ruiz-Ortiz, P.A., 2018. Facies analysis and stratigraphy of a lower Aptian carbonate platform section (Prebetic, Alicante, Spain) Estratigrafía y análisis de facies de una sección de una plataforma de carbonatos del Aptiense inferior (Prebético, Alicante, España). GEOGACETA 64. www.geogaceta.com.
Martínez-Rodríguez, R., Selby, D., Castro, J.M., de Gea, G.A., Nieto, L.M., Ruiz-Ortiz, P. A., 2021. Tracking magmatism and oceanic change through the early Aptian Anoxic Event (OAE 1a) to the late Aptian: Insights from osmium isotopes from the westernmost Tethys (SE Spain) Cau Core. Global Planet. Change 207, 103652. https://doi.org/10.1016/J.GLOPLACHA.2021.103652.
McAnena, A., Flögel, S., Hofmann, P., Herrle, J.O., Griesand, A., Pross, J., Talbot, H.M., Rethemeyer, J., Wallmann, K., Wagner, T., 2013. Atlantic cooling associated with a marine biotic crisis during the mid-cretaceous period. Nature Geoscience 2013 6:7 6 (7), 558–561. https://doi.org/10.1038/ngeo1850.
Méhay, S., Keller, C.E., Bermasconi, S.M., Weissert, H., Erba, E., Bottini, C., Hochuli, P. A., 2009. A volcanic CO2 pulse triggered the cretaceous Oceanic Anoxic Event 1a and a biocalcification crisis. Geology 37 (9), 819–822. https://doi.org/10.1130/G30100A.1.
Meyers, S.R., 2019. Cyclostratigraphy and the problem of astrochronologic testing. Earth-Science Reviews 190, 190–223. https://doi.org/10.1016/J.EARSCIREV.2018.11.015.
Meyers, S.R., Sageman, B.B., 2007. Quantification of deep-time orbital forcing by average spectral misfit. Am. J. Sci. 307 (5), 773–792. https://doi.org/10.2475/05.2007.01.
Moiroud, M., Martinez, M., Deconinck, J.-F., Monna, F., Pellenard, P., Riquier, L., Company, M., 2012. High-resolution clay mineralogy as a proxy for orbital tuning: Example of the Hauterivian–Barremian transition in the Betic Cordillera (SE Spain). Sediment. Geol. 282, 336–346. https://doi.org/10.1016/j.sedgeo.2012.10.004.
Moullade, M., Tronchetti, G., Granier, B., Bornemann, A., Kuhnt, W., Lorenzen, J., 2015. High-resolution integrated stratigraphy of the OAE1a and enclosing strata from core drillings in the Bedoulian stratotype (Roquefort-La Bedoule, SE France). Cretaceous Res. 56, 119–140.
Naafs, B.D.A., Castro, J.M., De Gea, G.A., Quijano, M.L., Schmidt, D.N., Pancost, R.D., 2016. Gradual and sustained carbon dioxide release during Aptian Oceanic Anoxic Event 1a. Nature Geoscience 2016 9:2 9 (2), 135–139. https://doi.org/10.1038/ngeo2627.
O'Brien, C.L., Robinson, S.A., Pancost, R.D., Sinninghe Damsté, J.S., Schouten, S., Lunt, D.J., Alsenz, H., Bornemann, A., Bottini, C., Brassell, S.C., Farnsworth, A., Forster, A., Huber, B.T., Inglis, G.N., Jenkyns, H.C., Linnert, C., Littler, K., Markwick, P., McAnena, A., Wrobel, N.E., 2017. Cretaceous sea-surface temperature evolution: Constraints from TEX86 and planktonic foraminiferal oxygen isotopes. Earth Sci. Rev. 172, 224–247. https://doi.org/10.1016/J.EARSCIREV.2017.07.012.
Ogg, J.G. Hinnov, L.A., Huang, C., Chapter 27 - Cretaceous, Editor(s): Felix M. Gradstein, James G. Ogg, Mark D. Schmitz, Gabi M. Ogg, The Geologic Time Scale, Elsevier, 2012, Pages 793-853, ISBN 9780444594259, https://doi.org/10.1016/B978-0-444-59425-9.00027-5.
Park, J., Oglesby, R.J., 1991. Milankovitch rhythms in the cretaceous: a GCM modelling study. Palaeogeography, Palaeoclimatology, Palaeoecology 90 (4), 329–355. https://doi.org/10.1016/S0031-0182(12)80034-4.
Pisias, N.G., 1983. Geologic time series from deep-sea sediments: Time scales and distortion by bioturbation. Mar. Geol. 51 (1–2), 99–113. https://doi.org/10.1016/0025-3227(83)90091-9.
R Core Team, 2013. R: A Language and Environment for Statistical Computing. R Foundation for Statistical Computing.
Rubino, J.-L., 1989. Introductory remarks on Upper Aptian to Albian siliciclastic/carbonate depositional sequences. In: Ferry, S., Rubino, J.-L. (Eds.), Mesozoic Eustacy on Western Tethyan Margins. Post-Meeting Field Trip in the "Vocontian Trough". ASF, Publ, pp. 28–45 (Spéc. 12).
Ruiz-Ortiz, P.A., Castro, J.M., de Gea, G.A., Jarvis, I., Molina, J.M., Nieto, L.M., Pancost, R.D., Quijano, M.L., Reolid, M., Skelton, P.W., Weissert, H.J., 2016. New drilling of the early Aptian OAE1a: the Cau core (Prebetic Zone, South-Eastern Spain). Sci. Drill. 21, 41–46. https://doi.org/10.5194/SD-21-41-2016.
Santos, A., De Lira Mota, M.A., Kern, H.P., Fauth, G., Paim, P.S.G., Netto, R.G., Sedorko, D., Lavina, E.L.C., Krahl, G., Fallgatter, C., Silveira, D.M., Aquino, C.D., Santos, M.O., Baecker-Fauth, S., Vieira, C.E.L., 2022. Earlier onset of the early cretaceous Equatorial humidity belt. Global Planet. Change 208, 103724. https://doi.org/10.1016/J.GLOPLACHA.2021.103724.
Schulz, M., Mudelsee, M., 2002. REDFIT: estimating red-noise spectra directly from unevenly spaced paleoclimatic time series. Comput. Geosci. 28 (3), 421–426. https://doi.org/10.1016/S0098-3004(01)00044-9.
Scott, R.W., 2014. A cretaceous chronostratigraphic database: construction and applications. Carnets de Géologie (Notebooks on Geology). https://doi.org/10.4267/2042/53522.
Scott, R., 2016. Barremian-Aptian-Albian carbon isotope segments as chronostratigraphic signals: Numerical age calibration and durations. Stratigraphy 13, 21–47.
Selby, D., Mutterlose, J., Condon, D.J., 2009. U–Pb and Re–Os geochronology of the Aptian/Albian and Cenomanian/Turonian stage boundaries: Implications for timescale calibration, osmium isotope seawater composition and Re–Os systematics in organic-rich sediments. Chem. Geol. 265 (3–4), 394–409. https://doi.org/10.1016/J.CHEMGEO.2009.05.005.
Sinnesael, M., De Vleeschouwer, D., Coccioni, R., Claeys, P., Frontalini, F., Jovane, L., Savian, J.F., Montanari, A., 2016. High-resolution multiproxy cyclostratigraphic analysis of environmental and climatic events across the Cretaceous-Paleogene boundary in the classic pelagic succession of Gubbio (Italy). Special Paper of the Geological Society of America 524, 115–137. https://doi.org/10.1130/2016.2524(09).
Skelton, P.W., Gili, E., 2012. Rudists and carbonate platforms in the Aptian: a case study on biotic interactions with ocean chemistry and climate. Sedimentology 59 (1), 81–117. https://doi.org/10.1111/J.1365-3091.2011.01292.X.
Skelton, P., Spicer, R.A., Kelley, S.P., Gilmour, I., 2003. In: Skelton, P.W. (Ed.), The Cretaceous World. Cambridge University Press for The Open University.
Skelton, P.W., Castro, J.M., Ruiz-Ortiz, P.A., 2019. Aptian carbonate platform development in the Southern Iberian Palaeomargin (Prebetic of Alicante, SE Spain). BSGF - Earth Sciences Bulletin 190, 3. https://doi.org/10.1051/BSGF/2019001.
Stein, M., Föllmi, K.B., Westermann, S., Godet, A., Adatte, T., Matera, V., Fleitmann, D., Berner, Z., 2011. Progressive palaeoenvironmental change during the Late Barremian–Early Aptian as prelude to Oceanic Anoxic Event 1a: Evidence from the Gorgo a Cerbara section (Umbria-Marche basin, central Italy). Palaeogeography, Palaeoclimatology, Palaeoecology 302 (3–4), 396–406. https://doi.org/10.1016/J.PALAEO.2011.01.025.
Steuber, T., Alsuwaidi, M., Hennhoefer, D., Sulieman, H., AlBlooshi, A., McAlpin, T.D., Shebl, H., 2022. Environmental change and carbon-cycle dynamics during the onset of cretaceous oceanic anoxic event 1a from a carbonate-ramp depositional system, Abu Dhabi, U.A.E. Palaeogeography, Palaeoclimatology, Palaeoecology 601, 111086. https://doi.org/10.1016/J.PALAEO.2022.111086.
Thibault, N., Perdiou, A., 2018. Reply to the discussion on 'Orbital calibration of the late Campanian carbon isotope event in the North Sea', Journal of the Geological Society, London, 173, 504–517. Journal of the Geological Society 175. https://doi.org/10.1144/jgs2018-001 jgs2018–001.
Thomson, D.J., 1982. Spectrum estimation and harmonic analysis. Proc. IEEE 70 (9), 1055–1096. https://doi.org/10.1109/PROC.1982.12433.
Thomson, D.J., 1990. Quadratic-Inverse Spectrum estimates: applications to Palaeoclimatology. RSPTA 332 (1627), 539–597. https://doi.org/10.1098/RSTA.1990.0130.
Tribovillard, N.P., 1989. Sédimentation rythmique dans les marnes bleues de l'Aptien-Albiendu Bassin vocontien (Sud-Est de la France). Geobios 22 (Suppl. 1), 213–224. https://doi.org/10.1016/S0016-6995(89)80058-0.
Tribovillard, N.P., Gorin, G.E., 1991. Organic facies of the early Albian Niveau Paquier, a key black shales horizon of the Marnes Bleues formation in the Vocontian Trough (Subalpine Ranges, SE France). Palaeogeogr. Palaeoclimatol. Palaeoecol. 85 (3–4), 227–237. https://doi.org/10.1016/0031-0182(91)90162-K.
Tuenter, E., Weber, S.L., Hilgen, F.J., Lourens, L.J., 2003. The response of the African summer monsoon to remote and local forcing due to precession and obliquity. Global Planet. Change 36 (4), 219–235. https://doi.org/10.1016/S0921-8181(02)00196-0.
Tuenter, E., Weber, S.L., Hilgen, F.J., Lourens, L.J., Ganopolski, A., 2005. Simulation of climate phase lags in response to precession and obliquity forcing and the role of vegetation. Climate Dynam. 24 (2–3), 279–295. https://doi.org/10.1007/S00382-004-0490-1/FIGURES/11.
Vera, J.A., 2001. Evolution of the Southern Iberian Continental margin. In: Ziegler, P., Cavazza, W., Robertson, A.F.H., Craquin-Soleau, S. (Eds.), Peri-tethys Memoir 6: Peri-Tethyan Rift-Wrench Basins and Passive Margins (Vol. 186, Pp. 109–143) (Mémoires du Muséum National d'Histoire naturelle).
Vera, J.A., 2004. In: Vera (Ed.), Geología de España. SGE-IGME.
Westerhold, T., Marwan, N., Drury, A.J., Liebrand, D., Agnini, C., Anagnostou, E., Barnet, J.S.K., Bohaty, S.M., De Vleeschouwer, D., Florindo, F., Frederichs, T., Hodell, D.A., Holbourn, A.E., Kroon, D., Lauretano, V., Littler, K., Lourens, L.J., Lyle, M., Pälike, H., et al., 2020. An astronomically dated record of Earth's climate and its predictability over the last 66 million years. Science 369 (6509), 1383–1388. https://doi.org/10.1126/SCIENCE.ABA6853/SUPPL_FILE/ABA6853_TABLES_S8_S34.XLSX.
Westermann, S., Stein, M., Matera, V., Fiet, N., Fleitmann, D., Adatte, T., Föllmi, K.B., 2013. Rapid changes in the redox conditions of the western Tethys Ocean during the early Aptian oceanic anoxic event. Geochim. Cosmochim. Acta 121, 467–486. https://doi.org/10.1016/J.GCA.2013.07.023.